



# Unravelling the role of hydrogen peroxide in pH-dependent ORR performance of Mn-N-C catalysts

Yuan Li<sup>1</sup>, Miao-Ying Chen<sup>1</sup>, Bang-An Lu<sup>\*</sup>, Hao-Ran Wu, Jia-Nan Zhang<sup>\*</sup>

College of Materials Science and Engineering, Zhengzhou University, Zhengzhou 450001, PR China

## ARTICLE INFO

### Keywords:

Oxygen reduction reaction  
PGM-free catalysts  
pH effects  
Hydrogen peroxide  
Degradation

## ABSTRACT

Although the Mn-N-C catalyst has low toxicity and high durability, its intense pH-dependent ORR activity is perplexing and prevents its commercial use in PEMFCs. Herein, we have developed a novel understanding of the role of hydrogen peroxide in the pH-dependent activity and stability of Mn-N-C catalysts. Instead of nitrogen protonation, the strong pH effects of ORR activity are caused by the much faster kinetics of the H<sub>2</sub>O<sub>2</sub> reduction reaction in alkaline medium than in acid, due to the lower dissociation energy of the HO-OH bond in alkaline environment. Regarding durability, the deactivation induced by H<sub>2</sub>O<sub>2</sub> demonstrates a strong pH dependence, primarily due to the differing intensities of reactive oxygen species at different pH values. Correspondingly, isopropanol effectively reduces Fenton reagents and increases the acid resistance of Mn-N-C sites. The present research provides a mechanistic understanding of pH effects and paves the way for the creation of more efficient catalysts.

## 1. Introduction

The exploration of platinum group metal-free (PGM-free) electrocatalysts with high activity towards oxygen reduction reaction (ORR) is vital for large-scale applications of fuel cells [1–4]. Nonetheless, under the proton exchange membrane fuel cell (PEMFC) operating conditions, the Fe-N-C catalysts regarded as the most promising PGM-free catalysts for ORR have demonstrated over 50% performance loss within the first 100 h due to their poor electrochemical stability, which is well below the minimum requirement for portable power applications [5–8]. This creates an excellent opportunity to seek out novel pyrolyzed catalysts other than Fe-N-C catalysts, which are severely affected by the Fenton reaction [8–10]. Specifically, the Fe centers catalyze the formation of highly active reactive oxygen species (ROS) from the reaction intermediate H<sub>2</sub>O<sub>2</sub>, which then assaults the carbon substrate, resulting in rapid activity degradation [6,11–13]. Given that ROS-induced deterioration is inherent to the catalysts, the durability issue can only be handled if the Fenton reaction can be greatly reduced, for example by employing less Fenton-reactive metal components [14–16].

As less Fenton-reactive reagents, Mn-N-C catalysts have garnered considerable interest, and significant advances have been made in synthesis techniques and performance enhancement [15,16]. Until now,

Mn-N-C catalysts have demonstrated greater activity on RDE in alkaline media, but much poorer performance in acid and, most notably, a lower power density than the benchmark Fe-N-C catalysts used in membrane electrode assembly (MEA) experiments. Understanding the intriguing but perplexing strong pH-dependent activity is beneficial to the rational design of high-performance Mn-N-C catalyst [17–23]. Currently, two hypotheses were proposed to address such performance gap: (1) the protonation of coordinated N atoms under acidic conditions results in activity degradation; (2) inner-sphere electron transfer is promoted in alkaline media and the competing two-electron ORR pathway for H<sub>2</sub>O<sub>2</sub> formation is suppressed, thereby enhancing their facilitation of the ORR process [20,24–29]. Also, different intrinsic intermediates may cover Fe-N-C in different pH solutions, and Li's team [30] suggests that \*O intermediates can better control the electronic structures of Fe-N-C catalysts in alkaline media. However, to the best of our knowledge, a direct explanation for the higher ORR activity of Mn-N-C catalysts under alkaline conditions has not been thoroughly disclosed.

Molecular manganese (II) naphthenate (MnPc) possesses an MnN<sub>4</sub> active site structure similar to practical pyrolyzed Mn-N-C catalysts for the acidic ORR, making it an ideal model system to derive the pH effects of such catalysts [17,31,32]. In this study, Mn-N-C catalyst was synthesized by loading MnPc molecules onto porous carbon black followed

<sup>\*</sup> Corresponding authors.

E-mail addresses: [balu@zzu.edu.cn](mailto:balu@zzu.edu.cn) (B.-A. Lu), [zjn@zzu.edu.cn](mailto:zjn@zzu.edu.cn) (J.-N. Zhang).

<sup>1</sup> Yuan Li and Miao-Ying Chen contributed equally.

by heated at 300 °C (denoted as MnPc/C-300). We found that the pH value has a substantial impact on the ·OH affinity on Mn centers, as well as the activity and stability of ORR. The half-wave potential ( $E_{1/2}$ ) shifts by 300 mV from 0.55 V at pH = 1 to 0.85 V in an alkaline medium with a pH = 13, primarily as a result of the altered ·OH affinity. On the basis of the results of controlled experiments, we suggested that the protonation of pyrrolic N cannot account for the enormous difference in catalytic activity between acidic and alkaline media, and that the strong pH effects of ORR activity result from the significantly faster electroreduction kinetics of  $H_2O_2$  in alkaline media than in acid. DFT calculations suggest that the HO-OH bond undergoes easier dissociation in an alkaline environment, leading to a subsequent reduction in the formation energy of  $H_2O$ . Additionally, the  $H_2O_2$ -induced deactivation reveals a strong pH-dependence, primarily due to the different intensity of ROS at various pH values. As a result, isopropanol, a powerful ROS scavenger, can significantly alleviate Fenton effects and enhance acidic ORR performance. This study elucidates the significance of  $H_2O_2$  in the pH effect and offers design guidelines for future Mn-N-C catalysts.

## 2. Experimental

### 2.1. Chemicals and materials synthesis

#### 2.1.1. Chemicals

Manganese phthalocyanine (MnPc, AR, Sigma-Aldrich), Ethanol (EtOH, Sinopharm), Ketjen black EC600JD carbon black (KJ600, Akzo Nobel), Isopropanol (IPA, AR, Macklin), Potassium hydroxide (KOH, ≥85%, Sinopharm), Sodium nitrite ( $NaNO_2$ , 99%, Sinopharm), Perchloric acid ( $HClO_4$ , 70%, Sinopharm), Sulfuric acid ( $H_2SO_4$ , AR, Sinopharm), Potassium permanganate ( $KMnO_4$ , ≥99%, Aladdin), and Nafion solution (D520, 5 wt%, Dupont) were used as received. All solutions were prepared with Ultrapure water (18.2 MΩ cm).

#### 2.1.2. Synthesis of MnPc/C catalyst

First, 20 mg MnPc and 60 mg KJ-600 were dissolved in 20 mL EtOH, respectively. After ultrasonic treatment at room temperature for 1 h, the two solutions were mixed, ultrasonic treatment for 1 h, stirring for 2 h. Next, the mixture is spin dried and then placed in a 60 °C oven overnight to obtain the dried product MnPc/C catalyst.

#### 2.1.3. Synthesis of MnPc/C-300, MnPc/C-600, and MnPc/C-800 catalysts

MnPc/C-300 catalysts were obtained by simple one-step pyrolysis of MnPc/C catalyst at 300 °C under 5 v%  $H_2$ /Ar for 2 h, respectively. The following temperature programming was used: the temperature was firstly increased from room temperature to target temperature at a rate of 10 °C min<sup>-1</sup>, and held at target temperature for 1 h, finally cooled to room temperature naturally. MnPc/C-600 and MnPc/C-800 catalysts was prepared using similar process, with the exception that the pyrolysis temperatures were 600 and 800 °C, respectively.

### 2.2. Characterization

The Scanning electron microscope (SEM) was performed with Zeiss Merlin Compact. The transmission electron microscope (TEM) and elemental mapping were acquired on FEI Tecnai G220 with an electron acceleration voltage of 200 kV. Aberration-corrected high-angle annular dark-field scanning transmission electron microscopy (AC-HAADF-STEM) images were recorded on a Titan 80–300 scanning/transmission electron microscope operated at 300 kV, equipped with a probe spherical aberration corrector. X-ray diffraction (XRD) measurements were characterized by X'Pert PRO X-ray Diffractometer using copper Kα radiation ( $\lambda = 1.5406 \text{ \AA}$ ) at 40 kV, 40 mA. X-ray photoelectron spectroscopy (XPS) measurements were performed on an ESCA LAB 250 spectrometer using Al Kα irradiation. Ultraviolet photoelectron spectroscopy (UPS) measurements were performed on Thermo Nexsa. Electron paramagnetic resonance (EPR) measurements were performed on

Bruker EMX plus. Raman measurements were performed on Thermo DXR 2xi. The manganese concentrations were conducted on the Agilent 5110 ICP-OES. X-ray absorption fine structure (XAFS) spectroscopy was carried out using the RapidXAFS 2 M (Anhui Absorption Spectroscopy Analysis Instrument Co., Ltd.) by transmission (or fluorescence) mode at 20 kV and 20 mA, and the Si (440) spherically bent crystal analyzer with a radius of curvature of 500 mm was used for Mn.

### 2.3. Electrochemical test

#### 2.3.1. Catalysts ink

The homogeneous catalyst ink was prepared by sonicating the mixture of 1 mg of catalyst, 250 μL of IPA, 140 μL deionized water, and 10 μL of Nafion solution (5 wt%) for 0.5 h. A thin film catalyst layer (0.125 mg cm<sup>-2</sup> catalyst) was obtained by depositing 10 μL of catalyst ink onto the rotating disk electrode (RDE, 0.2 cm<sup>-2</sup>).

#### 2.3.2. RDE tests

The electrochemical experiments were performed on an electrochemical workstation (CHI 760E) using a three-electrode system, with the RDE serving as the working electrode, the carbon rod as the counter electrode, and the saturated calomel electrode as the reference electrode. All potentials reported in this study were calibrated relative to the reversible hydrogen electrode (RHE). Before the experiments,  $N_2$  was bubbled for at least 30 min to ensure that the electrolyte was saturated by  $N_2$ . Then, cyclic voltammetry (CV) was performed to activate the catalysts completely. After that, RDE were conducted at 1600 rpm in an  $O_2$ -saturated electrolyte. Notably, the alkaline electrochemistry experiments were conducted in a plastic electrochemical cell in order to avoid contamination caused by the dissolution of glass in the strong alkaline media. Before tests, each cell was soaked in a solution of  $KMnO_4$  and  $H_2SO_4$  to eliminate all traces of the contaminant, and then rinsed thoroughly with deionized water.

#### 2.3.3. Rotating ring disk electrode (RRDE) tests

During the ORR process, the  $H_2O_2$  intermediate would diffuse from the disk electrode to the Pt ring. The potential of the Pt ring was set to 1.5 V vs. RHE so that the diffused  $H_2O_2$  could be oxidized instantly at the Pt ring electrode. The peroxide yields ( $H_2O_2\%$ ) were calculated from the ring current ( $I_r$ ) and the disk current ( $I_d$ ) using the following equation:

$$H_2O_2\% = \frac{200 \times I_r}{(I_r + N \times I_d)}$$

The electron transfer number ( $n$ ) in acid was calculated by the equation:

$$n = \frac{4 \times I_d}{(I_d + I_r/N)}$$

where  $N = 0.4$  is the current collection efficiency of the Pt ring.

#### 2.3.4. Chronoamperometry tests

To evaluate the electrochemical stability of the catalysts, stability experiments were carried out in  $O_2$ -saturated 0.1 mol L<sup>-1</sup>  $HClO_4$  or KOH. With a rotational speed of 1600 rpm, a constant potential was maintained on the disk electrode.

#### 2.3.5. The SD obtained by the method of nitrite

Using the nitrite method, the active site density SD of manganese atoms was determined. After poisoning the catalyst with  $NaNO_2$ , the active site density was determined by measuring the accumulation of cathode charge ( $Q_{strip}$ ) after nitrite absorption. The calculation formula is as follows:

$$SD[\text{sites nm}^{-2}] = \frac{Q_{strip} [C \text{ g}^{-1}] \times NA [\text{mol}^{-1}]}{n_{strip} F [C \text{ mol}^{-1}] \times SA [\text{nm}^2 \text{ g}^{-1}]}$$

Where  $Q_{\text{strip}}$  is the excess coulometric charge associated with the stripping peak,  $n_{\text{strip}} = 5$  is the number of electrons associated with the reduction of one nitrite per site, and SA is the surface area of the material.

### 2.3.6. Density functional theory (DFT) calculation

In this theoretical study, all geometric optimizations and energetic calculations were performed using spin-polarized density functional approach as implemented in the CP2K package [33]. Mn-containing compounds as a strongly correlated system, however, the Mn-3d electronic configuration can be correctly described in this calculation so we didn't include DFT+U method for Mn atom. Exchange-correction energies computational models were calculated using the generalized-gradient approximated Perdew–Burke–Ernzerh functional (GGA-PBE) [34,35]. Dispersion interaction was calculated by using the empirical parameterized Grimme (D3) method [36]. The valence-shell electrons ( $2s^2 2p^2$  for C,  $2s^2 2p^3$  for N,  $2s^2 2p^4$  for O, and  $3s^2 3p^6 3d^5 4s^2$  for Mn) are described using hybrid Gaussian and plane-wave (GPW) basis sets [37], that are at triple- $\zeta$  valence plus polarization function (TZVP) level with minimizing basis set superposition errors [38]. The cutoff energy of 600 Rydberg of auxiliary plane wave basis sets were adopted. Core-shell electrons of all elements were described using the Norm-conserving and separable Goedecker-Teter-Hutter (GTH) pseudopotentials [39]. Transition states of elementary reaction were computed by using the climbing image nudged-elastic-band method (CI-NEB) with a convergence criterion of 0.05 eV/Å [40]. Thermodynamic (Helmholtz) free energies were calculated,

$$A = E(\text{SCF}) + E_{\text{ZPE}} - TS.$$

where,  $E(\text{SCF})$  is the total electronic energy,  $E_{\text{ZPE}}$  represents zero-point energy, and  $S$  is the entropy of our model system that was approximately calculated only considering the vibrational contribution to the partition function for it,

$$S = R \sum_i \left\{ \frac{\theta_{v_i}/T}{e^{\theta_{v_i}/T} - 1} - \ln(1 - e^{-\theta_{v_i}/T}) \right\}$$

where the summation runs over all vibrational modes,  $\theta_{v_i}$  is the vibrational temperature for each vibrational mode  $i$ ,  $\theta_{v_i} = h\nu_i/k_B$ ,  $k_B$  is Boltzmann constant,  $\nu_i$  is the corresponding vibrational frequency,  $h$  is Planck constant, and  $T = 298$  K. The translational and rotational contributions were only considered for gas molecules of the  $\text{H}_2\text{O}$  and  $\text{O}_2$ . The molecular vibration contribution to thermal energy is considered and calculated using the following equation:

$$E_v = R \sum_i \theta_{v_i} \left( \frac{1}{2} + \frac{1}{e^{\theta_{v_i}/T} - 1} \right)$$

Zero-point vibrational energies (ZPE) were calculated using the harmonic approximation according to the equation of  $E_{\text{ZPE}} = \frac{1}{2} \sum_i h\nu_i$ , where  $\nu_i$  is non-imaginary frequency.

## 3. Results and discussions

### 3.1. Structural characterization

The MnPc/C-300 catalyst was manufactured by homogeneously depositing MnPc molecules onto porous KJ-600 carbon black and then heating at 300 °C. During the ORR process, the MnPc molecule served as the catalytic site, while KJ-600 served as a conductive support with no detectable catalytic effect. The FTIR measurements reveal a high absorption peak at  $\sim 724 \text{ cm}^{-1}$ , which can be ascribed to the vibration of the MnPc molecule (Fig. S2), indicating that MnPc molecules have been successfully incorporated into the KJ-600 (Fig. S2 and Table S1). The

SEM analysis (Figs. S3–4) reveals that MnPc/C-T ( $T = 30, 300, 600$ , and  $800$  °C) has a similar morphology consisting of carbon nanoparticles (30–50 nm in diameter). The TEM image (Fig. S5) at high resolution reveals the MnPc/C-300 has a rugged surface, porous structure, and irregular shape. The aberration-corrected high-angle annular dark-field scanning transmission electron microscopy (AC-HAADF-STEM) picture is shown in Fig. 1b, and the bright spot indicates the presence of atomically dispersed Mn atoms in MnPc/C-300 catalyst. The presence of Mn, N, and C could also be identified by the electron energy loss spectrum (EELS) (Fig. 1c). In addition, Energy dispersive X-Ray spectroscopy (EDS) results (Fig. S6) reveals the content of C, N, O, and Mn elements in the catalyst, and STEM-EDS elemental mapping (Fig. S7) disclose that C, N, and Mn atoms are uniformly distributed throughout the catalyst without any aggregated Mn-containing particles [41]. Fig. S8 displays the XRD spectra of pristine MnPc/C and pyrolyzed MnPc/C-300. There is no metal diffraction peak when MnPc is deposited on KJ-600 carbon Black, indicating that MnPc is evenly distributed on the carbon carrier [41]. After heat treatment at 300 °C, only two broad peaks appear at 22° and 43°, which are attributed to carbon diffraction peaks. Simultaneously, no crystal diffraction peak related to manganese nanoparticles was observed, indicating that there were no metal particles in the MnPc/C-300 catalyst and that metal atoms were disseminated in the carbon material. MnPc/C-800 sample (Fig. S9) contained a manganese metal diffraction peak when the pyrolysis temperature reached 800 °C, suggesting that there are few metal nanoparticles, that MnPc molecules decompose at 800 °C, and that metal atoms tend to clump together to form particles.

The presence form of Mn and the coordination structure of  $\text{MnN}_4$  in the MnPc/C-300 catalyst were further investigated by X-ray absorption spectroscopy (XAS), including X-ray absorption near edge structure (XANES) and extended X-ray absorption fine structure (EXAFS) measurements at the Mn-K edge. The Mn Mn-K edge of the XANES spectrum (Fig. 1d) clearly shows the adsorption side of MnPc/C-300 between  $\text{MnO}$  and  $\text{Mn}_2\text{O}_3$ , indicating that the oxidation state of Mn in MnPc/C-300 is between +2 to +3. The Fourier transform (FT-EXAFS) results (Fig. 1e) show that the MnPc/C-300 catalyst is around 1.44 Å and the MnPc is around 1.53 Å, which is attributed to the scattering bonding of Mn-N. Around 2.3 Å, Mn-Mn has no contribution and can be found in both catalysts. In addition, the model further confirms the coordination structure of  $\text{MnN}_4$  of MnPc/C-300 based on EXAFS (Fig. S10 and Table S2). Based on the above analysis, it can be concluded that the Mn atom in the MnPc/C-300 catalyst is atomically embedded and coordinated with four N ligands.

To further elucidate the pyrolysis process of MnPc molecular, thermogravimetric (TG) measurements (Fig. S11) were undertaken on pure MnPc and MnPc/C-T [32,41,42]. Pure MnPc exhibits three significant mass loss peaks, primarily at 200, 350, and 600 °C. At 200 °C, the first mass loss peak indicates that MnPc molecules began to decompose and ligands broke apart. MnPc/C-300 exhibited the superior ORR activity after pyrolysis in an acidic medium when calcined at 300 °C, indicating that decomposition occurred only on the second shell group of  $\text{MnN}_4$  without destroying the Mn- $\text{N}_4$  structure [43,44]. According to TG data, the structure of  $\text{MnN}_4$  could be destroyed during pyrolysis at 600 °C (Fig. S11), and metal atoms without ligands are unstable, atomic order is difficult to distribute, and agglomeration occurs, which is consistent with XRD data [41].

The surface constituents and elemental functionalities of the MnPc/C-T series were investigated using XPS characterization [45]. As shown in Fig. S12, the XPS survey spectra of all the catalysts disclose the presence of C, N, O, and a trace amount of Mn. The percentages of C, N, O, and Mn are computed based on the respective peak areas of the high-resolution XPS (Table S3). When the temperature exceeds 300 °C, the Mn and N contents decrease significantly. The decreased heteroatom content can be attributed to the low thermal stability of MnPc molecules, which may decompose at elevated temperatures. Fig. S13 displays the Mn 2p spectra and the peak at 642.5 eV corresponds to the  $\text{Mn } 2p^{3/2}$

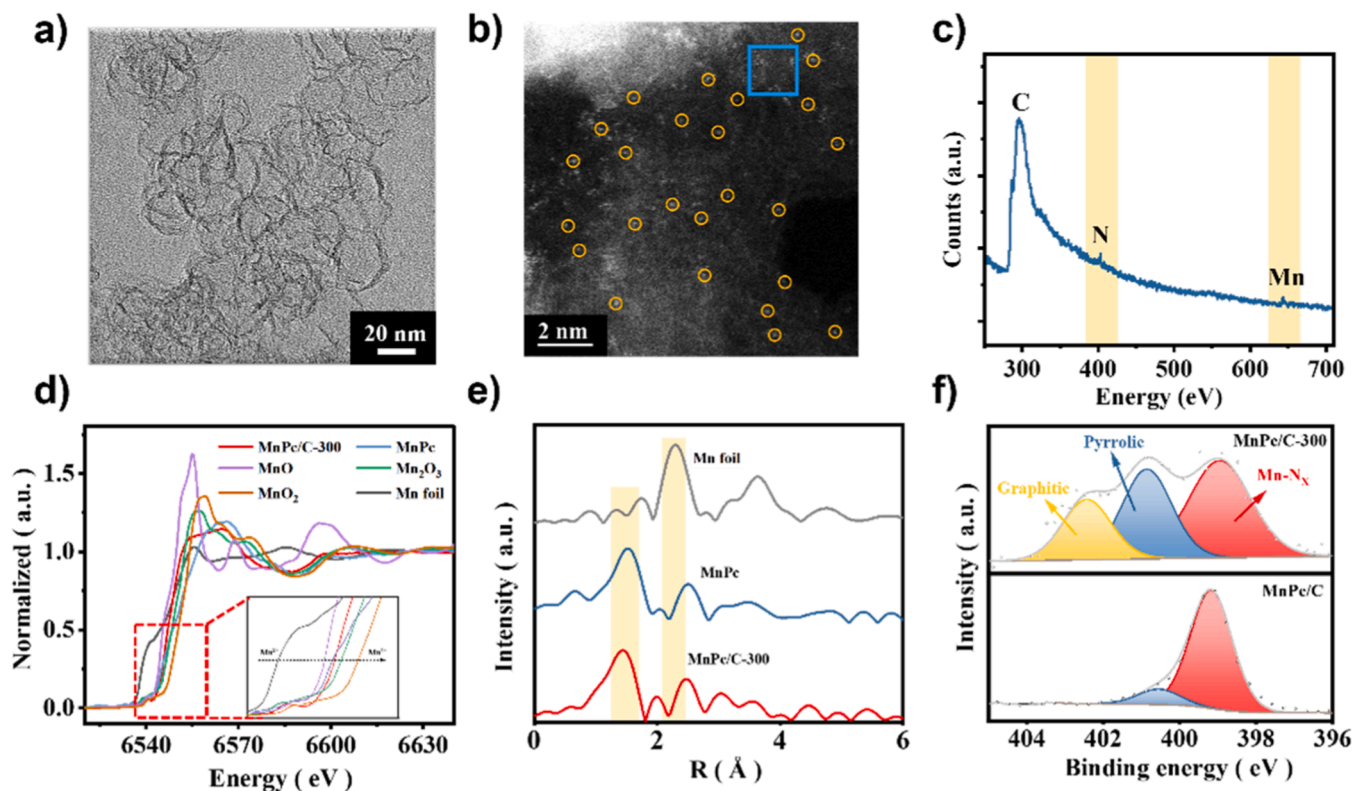


**Fig. 1.** The morphology and structure of catalysts. (a) TEM image of MnPc/C-300; (b) AC-HAADF-STEM of Mn single atom of MnPc/C-300 catalyst and (c) EELS of the recorded areas shown in Figure b; (d) The experimental K-edge XANES spectra of MnPc/C-300 catalyst and reference sample (Mn foil, MnO, Mn<sub>2</sub>O<sub>3</sub>, MnO<sub>2</sub>, MnPc); (e) Fourier transform of Mn-K edge EXAFS data for MnPc/C-300, MnPc and Mn Foil catalysts; (f) High-resolution N 1s XPS spectra of MnPc/C and MnPc/C-300 catalysts.

transition. As the temperature of pyrolysis rises, the peak intensity of Mn 2p spectra decreases. Due to the low concentration of Mn in MnPc/C-800 at temperatures above 800 °C, the spectrum of Mn 2p was somewhat chaotic (Fig. S14), making it difficult to resolve overlapping peak to distinguish specific chemical state of Mn. The typical N 1s spectra of pristine and pyrolyzed MnPc/C-T (T = 300–800 °C) at high resolution (Fig. S13, Fig. S14). It is evident that the N content varies considerably with pyrolysis temperature, particularly above 300 °C, where the formation of more gaseous N-containing phases causes the N content to decrease dramatically. Increasing the pyrolysis temperature not only reduces the total amount of N, but also alters the bonding configuration of N atoms. As seen in Fig. 1f, the N 1s XPS spectra of pristine MnPc/C can be deconvoluted into two peaks with binding energies of 398.92 eV and 400.8 eV, respectively, identified as metal-N and pyrrolic-N. MnPc/C-300 can be decomposed into three peaks with binding energies of 399.1, 400.6 eV, and 402.5 eV. These peaks correspond to metallic-N, pyrrolic-N, and graphitic-N, which may coordinate directly with edge carbon. It has been discovered that at lower temperatures, metallic-N accounts for the majority of total N. The pyrolysis temperature has a significant influence on the activity and structure of MnPc/C. The pristine MnPc/C catalyst delivers rather poor acidic activity but the alkaline  $E_{1/2}$  is recorded as 0.62 V (Fig. S15). However, the  $E_{1/2}$  of catalysts significantly decreased when the pyrolysis temperature increased to 800 °C, due to the decrease of Mn-N<sub>x</sub> species (Fig. S14) and the aggregation of Mn specie. Therefore, we select the 300 °C as the optimum pyrolysis temperature, which can gain the high activity as well as the retention of the structure of MnPc. According to extensive research, MnN<sub>4</sub> is the primary active site for pyrolyzed Mn-N-C catalysts in acidic medium [23,32,46,47]. In this study, samples pyrolyzed at 800 °C have a high graphitic N content but a low ORR activity.

Since it represents the minimum energy required for inner electrons to escape from solid catalysts, the work function ( $\phi$ ) could be one of the

crucial factors determining the electron transfer process [48,49]. A modest value suggests that it is simpler to activate electrons for chemical reactions. Consequently, the UPS spectra were used to examine the MnPc/C and MnPc/C-300 (Fig. S16). Intriguingly, the cutoff energy ( $E_{\text{cutoff}}$ ) of MnPc/C-300 and MnPc/C is 17.26 and 17.00 eV, respectively. It was calculated using the equation  $\phi = h\nu - E_{\text{cutoff}}$ , where  $h\nu$  (21.22 eV) is the incident photoenergy from the I excitation source. The  $\phi$  of MnPc/C-300 was estimated to be 3.96 eV, which is less than the value commonly reported for MnPc/C ( $\phi = 4.22$  eV). MnPc/C-300 with a lower energy barrier would manifest a stronger electron transfer to induce ORR than its counterpart, and ORR would occur more readily. In the Raman spectrum (Fig. S17), we observed the characteristic signature of nanocarbons, with the D band at 1350 cm<sup>-1</sup> and the G band at 1588 cm<sup>-1</sup> [22]. The nearly constant ratio of Raman spectra to G and D peaks indicates that the calcination temperature does not result in significant defects. The ICP-MS indicates that the Mn content of MnPc/C-300 can attain 1.75 wt% (Table S4), which is less than that of MnPc/C (2.87 wt%).

### 3.2. The pH effects of activity and stability

As a type of model molecular catalyst, MnPc macrocyclic compounds exhibit significant ORR activity in alkaline media [17]. The active site of MnN<sub>4</sub> is well-defined and uniform. Unlike pyrolyzed Mn-N-C catalysts, this material lacks complex porous structures and mass transfer issues. The MnPc molecule possesses an active site comparable to that of pyrolyzed Mn-N-C catalysts. It is possible to clarify the pH effects of molecular MnPc during the ORR process and then to approximate the actual decay profile of practical pyrolyzed Mn-N-C catalysts during the operation of PEMFCs.

In lieu of cyclic voltammetry (Fig. S18), we utilized square-wave voltammetry (SWV) to obtain a more precise identification of the peak



position, as a result of its high rejection of capacitive current and improved sensitivity to Faradaic processes [24,46]. As shown in Fig. 2a, the pH has a visible effect on the redox potential of  $\text{Mn}^{2+}/\text{Mn}^{3+}$ , suggesting an alteration of the  $\cdot\text{OH}$  binding energy. Interestingly, we observe a linear relationship with a slope of  $0.035 \text{ V pH}^{-1}$ , indicating that the  $\cdot\text{OH}$  binding energy was weakened at high pH values. Fig. 2b shows a comparison of the ORR polarization curves of MnPc/C-300 catalysts in  $\text{O}_2$ -saturated 0.1 M  $\text{HClO}_4$  and 0.1 M KOH solutions. Clearly, the ORR catalytic activity in alkaline medium is much higher than that in acid. The  $E_{1/2}$  is positively shifted by 300 mV from 0.550 mV at pH=1 to 0.850 mV at pH=13, which indicates that the ORR catalytic activity in alkaline medium is about 2–3 orders of magnitude higher than that in acid. Similarly, there is also a good linear correlation between pH and the catalytic activity of ORR (Fig. 2b) and the slope is  $0.023 \text{ V pH}^{-1}$ . These results demonstrate the strong pH-dependent ORR activity of MnPc/C-300. As shown in Fig. S20, MnPc/C also exhibits similar pH-dependent ORR performance, i.e., with  $E_{1/2} = 0.636 \text{ V}$  at pH=13, but no obvious activity at pH=1 [29,50–53]. Similarly, the ORR activity of commercial JM Pt/C catalysts showed a significant pH dependence, with  $E_{1/2} = 0.748 \text{ V}$  at pH=1 and  $E_{1/2} = 0.798 \text{ V}$  at pH=13 (Fig. S21 and Fig. S22). While the activity of MnPc/C-300 catalysts is considerably diminished in comparison to advanced M-N-C catalysts, it remains on par with that of other reported MPc catalysts [54–56].

We also notice that there is a good correlation between ORR performance and the peak position observed in SWV curves in Fig. 2a and b, suggesting that the effect on  $\cdot\text{OH}$  binding energy may dominate the change in ORR kinetics. Zagal et al. correlated the  $\text{M}^{\text{II}}/\text{M}^{\text{III}}$  redox potential of  $\text{MN}_4$  chelates and the  $\text{M}-\text{O}_2$  binding energies [17]. Specifically,

the  $\text{O}_2$  (and other O species) binding energy follows the  $\text{M}^{\text{III}}\text{-OH}/\text{M}^{\text{II}}$  (M is a transition metal element) redox transition for  $\text{MnN}_4$  and  $\text{FeN}_4$  chelates.  $\text{MnN}_4$  should lie on the strong-binding side of the Sabatier activity volcano, and weakening the  $\cdot\text{OH}$  bond has been discovered to increase the ORR activity, consistent with our results. This observation shows how the effect of pH depends not only the nature of the electronic structure, but also on that of the catalyst's ORR performance. A possible explanation of the effect of pH on the  $\cdot\text{OH}$  bond may originate from the different donor of  $\cdot\text{OH}$  under a wide pH range. Although we take the view that the effect on the  $\cdot\text{OH}$  bond has a strong influence on ORR kinetics, we cannot exclude the possibility that other factors might play an important role.

In the potential range of 0.2–0.6 V, the hydrogen peroxide yield of the MnPc/C-300 catalyst is less than 5% at pH=13 (Fig. 2c and Fig. 23), whereas  $\text{H}_2\text{O}_2\%$  is less than 15% at pH=1, indicating that  $\text{H}_2\text{O}_2$  are more readily generated under acidic conditions. Intriguingly, as the potential exceeds 0.6 V, the yield of hydrogen peroxide rises dramatically. In acid, the  $\text{H}_2\text{O}_2\%$  reaches 45% at 0.7 V, which is 75 times higher than in alkaline medium. Clearly, the yield of  $\text{H}_2\text{O}_2$  exhibits a strong pH dependence, particularly in the kinetic potential region of ORR. During ORR, the number of transfer electrons of the MnPc/C-300 catalyst also varies with pH (Fig. S23). The high yield of hydrogen peroxide generated may accumulate on the cathode side of fuel cells and severely degrade the performance and durability of fuel cells. As shown in Fig. S24–25, after MnPc/C-300 was treated with hydrogen peroxide, the polarization curve shifted negatively by 80 mV at pH=1 and 60 mV at pH=13, hydrogen peroxide yield increased, and selectivity decreased. Furthermore, in Fig. S26, after hydrogen peroxide treatment, the redox peak at 0.80 V decreases, indicating that hydrogen peroxide causes loss

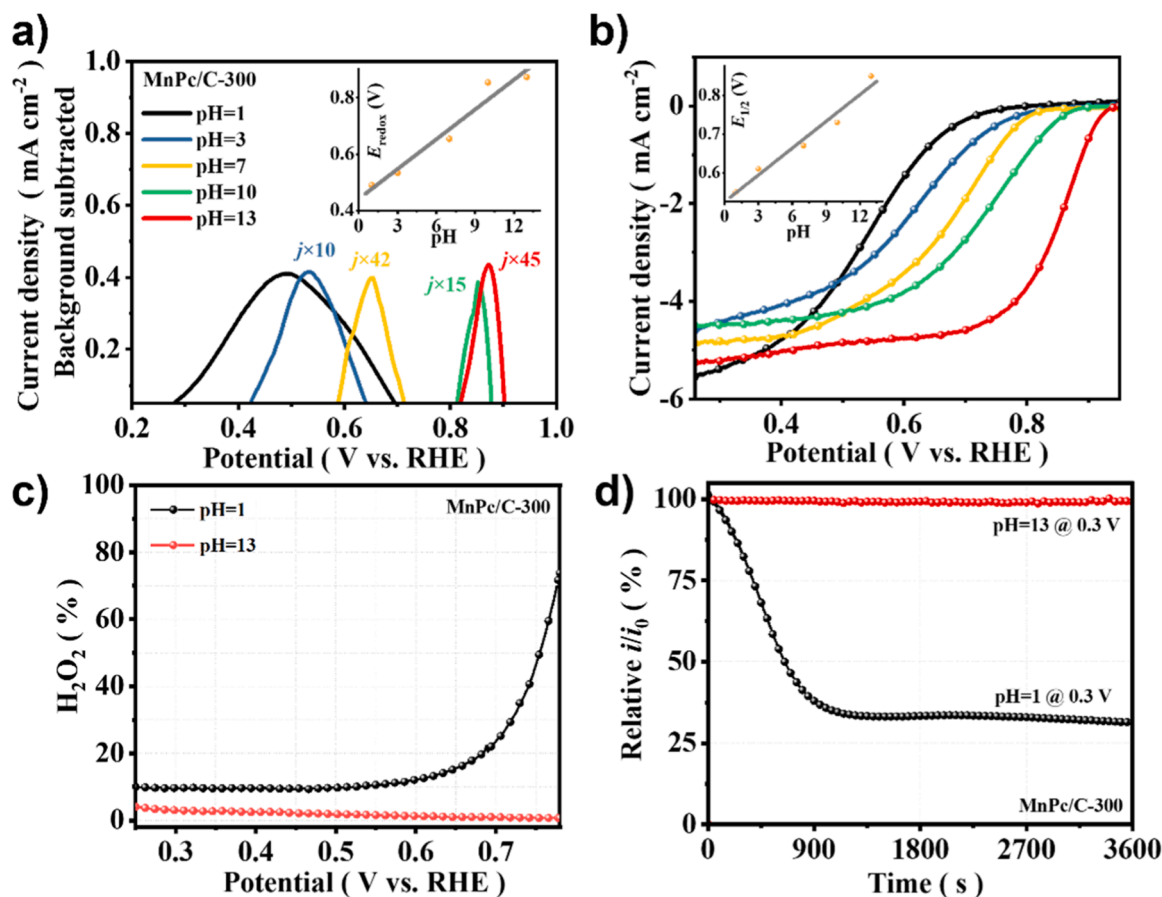


**Fig. 2.** The pH-dependent ORR performance. (a) SWV of MnPc/C-300 catalyst in  $\text{N}_2$ -saturated electrolyte with different pH. Inset: The fit curve of pH and  $E_{\text{redox}}$ . (b) Polarization curve of MnPc/C-300 catalyst in  $\text{O}_2$ -saturated electrolyte with different pH. Inset: The fit curve of pH and  $E_{1/2}$ . (c)  $\text{H}_2\text{O}_2$  yield of MnPc/C-300 catalyst at pH = 1 and pH = 13; (d) The  $i$ - $t$  curve of MnPc/C-300 catalyst operating at 0.3 V for 1 h in electrolytes pH = 1 and pH = 13.

of active sites, which is more severe in acid than in alkaline medium. This conclusion can also be supported by XPS of MnPc/C-300 catalyst before and after hydrogen peroxide treatment (Fig. S27 and Fig. 28).

Interestingly, we also observed a strong pH-dependent deactivation behavior of MnPc/C-300 catalysts. As shown in the chronoamperometry test (Fig. 2d), the current density at 0.3 V decreased to 31% of the initial values at pH=1. However, at pH=13, the catalyst current density almost remained unchanged. Similarly, comparing the stability of MnPc/C-300 catalyst at 0.6 V after 1 h of chronoamperometry test, the results showed that the current density of the MnPc/C-300 catalyst was close to 0 mA cm<sup>-2</sup> after 800 s at pH=1, while the current density decreased by only 8% in 1 h at 0.1 M KOH (Fig. S29). This suggests that MnPc/C-300 catalysts degrade when ORR occurs at pH=1. Similarly, Fig. S30 showed that MnPc/C-300 decreased by 150 mV in  $E_{1/2}$  after CV cycles in pH=1, while  $E_{1/2}$  remained basically unchanged in pH=13.

### 3.3. The origin of pH-dependent activity

#### 3.3.1. The impacts of acid, potential and O<sub>2</sub>

During the ORR, the pH effects of the MnPc/C-300 catalyst could be caused by a number of variables, such as protonation in an acidic environment, the O<sub>2</sub> atmosphere, potential cycles, and H<sub>2</sub>O<sub>2</sub> attack. The isolated experiments were conducted on each of these variables in order to determine the most significant factor responsible for the pH effects of the MnPc/C-300 catalyst. In order to evaluate the influence of acid/alkaline attack on catalyst, the ORR polarization curves of MnPc/C-300 catalysts before and after different treatments were recorded. As demonstrated in Fig. 3a, the ORR activity of MnPc/C-300 at pH=13 did

not change substantially before and after acid treatment, indicating that acid attack did not degrade the structure of catalysts. Fig. 3b demonstrates that alkaline attack did not diminish the activity of catalysts. We also investigated the effect of atmosphere on acid medium performance. After 100 potential cycles between 0.6 and 1.0 V under N<sub>2</sub> atmosphere, the ORR activity is nearly identical to its initial value. However, MnPc/C-300 demonstrated a dramatic decline in O<sub>2</sub>-saturated HClO<sub>4</sub>, even after multiple potential cycles.

Inspired by previous literature [27], we used the combination of Nafion and MnPc/C-300 to simulate an acidic environment during the XPS measurement because of their low volatility and stability under ultra-high vacuum conditions. XPS analysis revealed that MnPc/C-300 after Nafion treatment contained three varieties of nitrogen (Fig. 3d, Fig. S27-28, and Table S5). In contrast, the relative composition of nitrogen species is nearly unaffected after alkaline treatments. However, after acid treatments, the proportion of Mn-N<sub>x</sub> decreases from 37.55% to 14.59% and that pyrrolic-N decrease from 30.06% to 18.36%. Similar results are observed with protonation of pyridinic nitrogen in Fe-N-C electrocatalyst [5,27]. Intriguingly, even intense protonation occurred after acid treatments, but almost all of the ORR performance was preserved, as depicted in Fig. 3c. Based on the aforementioned findings, we suggested that protonation and acid attack may not account for the substantially poor performance of catalysts in acid. Instead, the intermediates generated by ORR in acid medium, such as H<sub>2</sub>O<sub>2</sub> or ·OH, can destruct the active sites, resulting in a performance decline.

#### 3.3.2. The pH-dependent redox reactions of H<sub>2</sub>O<sub>2</sub>

Hydrogen peroxide is an essential intermediate in ORR, serving a

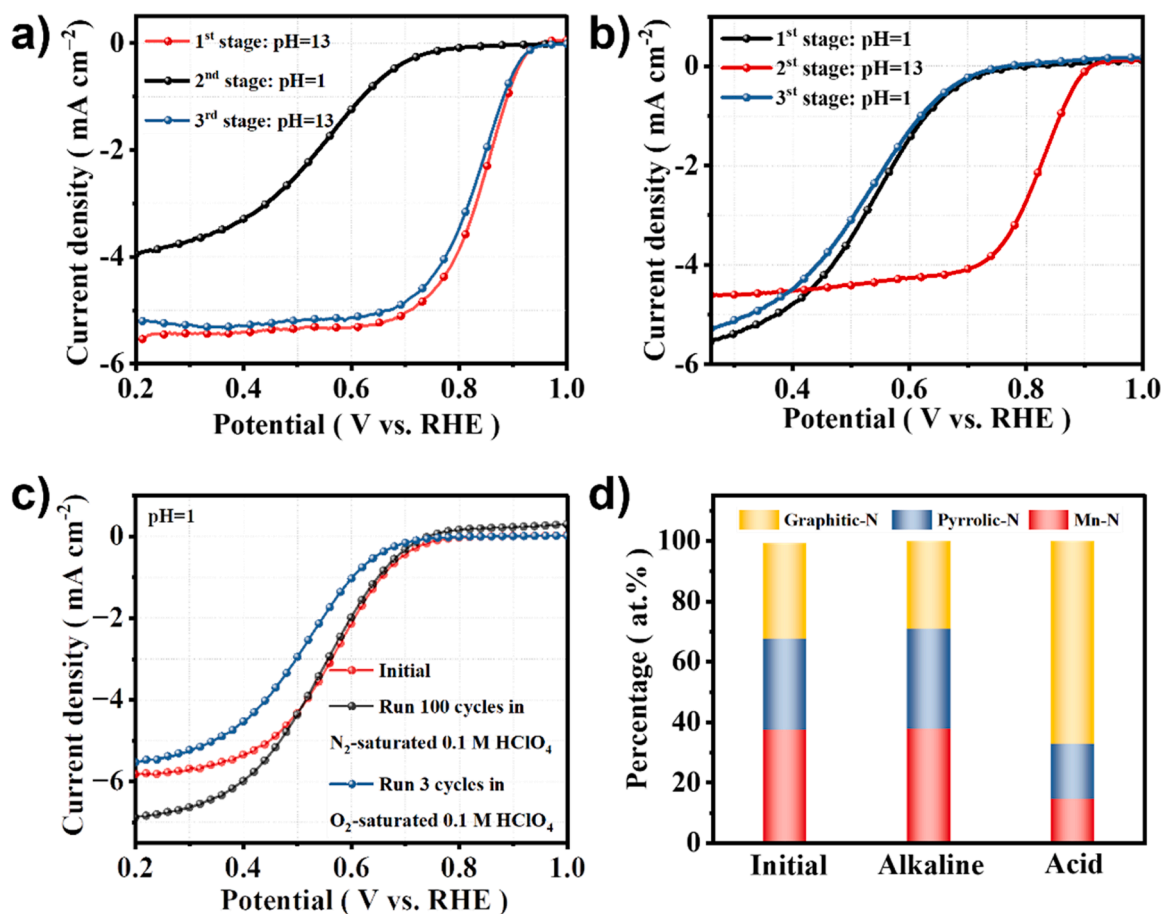


**Fig. 3.** The impacts of acid, potential and O<sub>2</sub>. (a) The influence of acid treatment on the activity of MnPc/C-300 in pH = 13; (b) The influence of alkaline treatment on the ORR activity of MnPc/C-300 in pH = 1; (c) The comparison of atmosphere effects of acid treatment on the activity of MnPc/C-300 in pH = 1; (d) The relative content of nitrogen types of MnPc/C-300 catalysts after different treatments.

crucial role in both the activity and stability of ORR [11,57,58]. Depending on the electrode potential,  $\text{H}_2\text{O}_2$  can either be reduced to water (hydrogen peroxide reduction reaction, HPOR),  $E^0 = 1.76$  V, or oxidized to  $\text{O}_2$  (hydrogen peroxide oxidation reaction, HPOR),  $E^0 = 0.695$  V [59]. The dual nature of this molecule makes it a valuable probe for building electrochemical models. As such, we investigated the reduction and oxidation of  $\text{H}_2\text{O}_2$  to better understand the pH-dependent ORR process. Cyclic voltammetry experiments were conducted in  $\text{N}_2$ -saturated electrolytes containing 1.0 wt%  $\text{H}_2\text{O}_2$ . Clearly,  $\text{H}_2\text{O}_2$  reduction (HPRR) and oxidation (HPOR) can occur within the broad potential range of  $-0.2$  to  $1.4$  V for  $\text{MnPc/C-300}$  catalysts (Fig. 4a and Fig. S31). Compared to  $\text{pH} = 13$ ,  $\text{MnPc/C-300}$  displayed a lower HPRR current and a higher HPOR current at  $\text{pH} = 1$ , indicating that it is more difficult for  $\text{MnPc/C-300}$  to further reduce hydrogen peroxide into water at  $\text{pH} = 1$  than at  $\text{pH} = 13$  (Fig. 4b). In addition, the pH influenced the onset potential ( $E_{\text{onset}}$ ) of HPRR.  $E_{\text{onset}}$  of HPRR was 290 mV more negative at  $\text{pH} = 1$  than at  $\text{pH} = 13$ , indicating that HPRR at  $\text{pH} = 1$  requires a less negative potential, while HPOR is more feasible. Consistent with previous findings, we also observed a dependence between  $\text{H}_2\text{O}_2$  concentration and  $E_{\text{onset}}$ , with  $E_{\text{onset}}$  rising with increasing  $\text{H}_2\text{O}_2$  concentration (Fig. S32) [60]. Furthermore, at  $\text{pH} = 1$ , the Tafel slope of HPRR is  $594 \text{ mV dec}^{-1}$ , and at  $\text{pH} = 13$ , it is  $111 \text{ mV dec}^{-1}$  (Fig. 4c). Fig. 4b illustrates that the current density of HPRR at  $0.7$  V is  $7.41 \text{ mA cm}^{-2}$  at a pH of 13, which is 18.7 times greater than the value at  $\text{pH} = 1$ . As indicated by the steeper slope of Tafel at  $\text{pH} = 1$ , hydrogen peroxide is more difficult to convert to water via the association mechanism and is more likely to accumulate at that pH than at  $\text{pH} = 13$ . In acidic media, HPOR kinetics are significantly quicker than in alkaline media. At  $\text{pH} = 1$ , the Tafel slope of HPOR is  $98 \text{ mV dec}^{-1}$ , whereas it is  $186 \text{ mV dec}^{-1}$  at  $\text{pH} = 13$ . In contrast with  $\text{pH} = 13$ , the Tafel slope is

significantly diminished at  $\text{pH} = 1$ , suggesting that HPOR kinetics occur at a quicker rate at  $\text{pH} = 1$ .

As shown in Fig. 4d, we further compared the pH effects on ORR activity, the onset potential of HPRR and the potential of  $\text{Mn}^{2+}/\text{Mn}^{3+}$ . We discovered that as pH increased, the redox potential of  $\text{Mn}^{2+}/\text{Mn}^{3+}$  shifted substantially in the positive direction. Similarly, the oxygen reduction activity and hydrogen peroxide reduction activity increased. These results indicate that the difference in  $\cdot\text{OH}$  binding energy may dominate the pH-dependent changes in ORR and HPRR kinetics. The applied potential determines the surface state of metal centers, which then determines the direction of  $\text{H}_2\text{O}_2$ 's redox reaction and the ensuing ORR kinetics. The kinetics of HPRR may originate from the surface's inherent affinity for oxygenated species. When  $\text{H}_2\text{O}_2$  interacts with reduced surface sites, such as  $\text{Mn}^{2+}$ , it decomposes into  $\cdot\text{OH}$  species that are adsorbed.  $\text{H}_2\text{O}_2$  is converted to  $\text{O}_2$  when it interacts with oxidized sites, such as  $\text{Mn}^{3+}$ , by reducing the surface. Hence, the rate of ORR and HPRR is governed by the pH-dependent oxidation of the surface state of Mn centers.

These results demonstrate conclusively that alkaline media are favored for HPRR, as any intermediate peroxide generated during ORR at  $\text{pH} = 13$  will be rapidly reduced to the  $4e^-$  product, i.e.,  $\text{H}_2\text{O}$ . However, the HPRR in acidic media is kinetically unfavorable due to the weak binding of  $\text{H}_2\text{O}_2$  to the active site, which leads to its desorption into the bulk electrolyte and/or catalytic decomposition into molecular  $\text{O}_2$ . In addition, the increased stability of the peroxide intermediate results in the so-called kinetic facility in alkaline medium, but not in acidic medium. As suggested by previous studies, alkaline media can function as a homogeneous catalyst to stabilize the  $\text{HO}_2^-$  intermediate [24]. Moreover, the pH effects may also be explained by the double-layer electrostatic effect. Taking into account the pKa values for the first

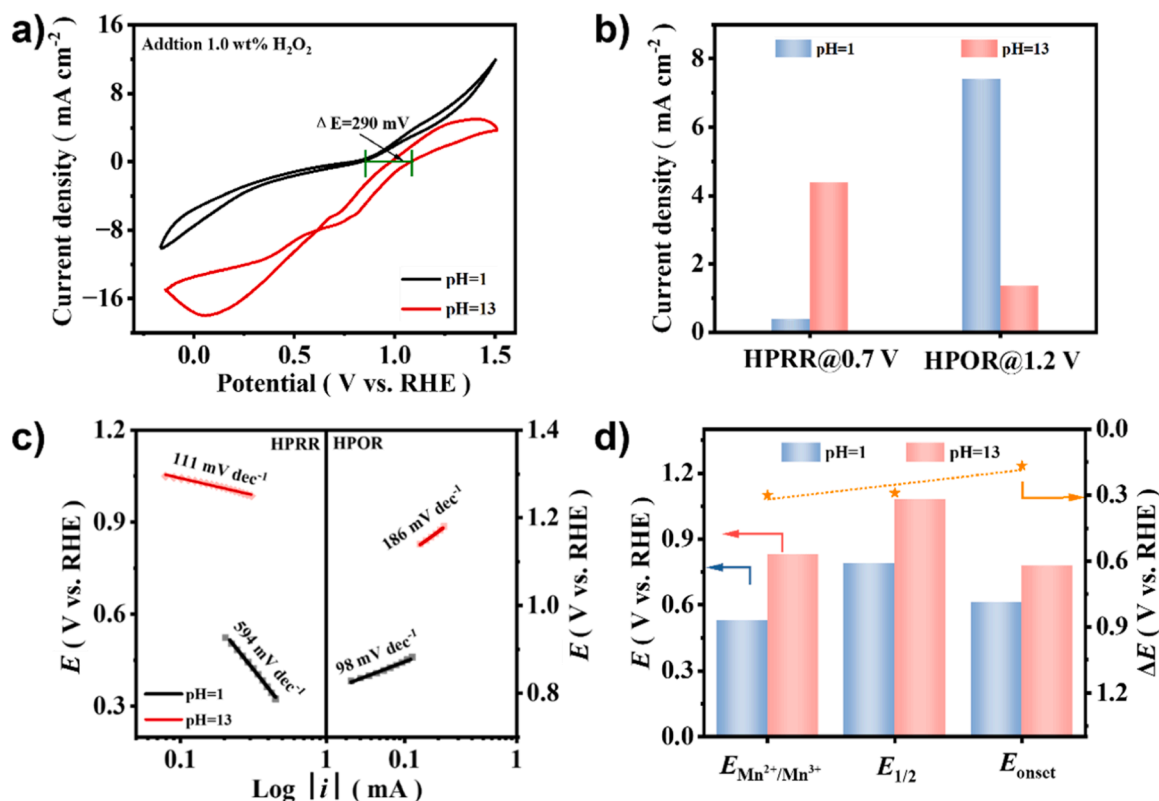


**Fig. 4.** The pH-dependent redox reactions of  $\text{H}_2\text{O}_2$ . (a) Cyclic voltammetry curves at  $\text{N}_2$ -saturated  $\text{pH} = 1$  and  $\text{pH} = 13$  electrolyte of  $\text{MnPc/C-300}$  catalysts containing 1.0 wt%  $\text{H}_2\text{O}_2$ , scan rate:  $10 \text{ mV s}^{-1}$ ; (b) The current densities at  $\text{N}_2$ -saturated  $\text{pH} = 1$  and  $\text{pH} = 13$  electrolyte containing 1.0 wt%  $\text{H}_2\text{O}_2$  of  $0.7$  and  $1.2$  V vs. RHE, respectively; (c) Tafel slope of HPRR and HPOR for  $\text{MnPc/C-300}$  catalyst with 1.0 wt%  $\text{H}_2\text{O}_2$  at  $\text{pH} = 1$  and  $\text{pH} = 13$  electrolyte; (d) The comparisons of  $E_{\text{onset}}$ ,  $E_{1/2}$ , and  $E_{\text{Mn}^{2+}/\text{Mn}^{3+}}$  for  $\text{MnPc/C-300}$  catalyst with 1.0 wt%  $\text{H}_2\text{O}_2$  at  $\text{pH} = 1$  and  $\text{pH} = 13$  electrolyte (left axis), and their corresponding potential difference between alkaline and acid (right axis), i.e.,  $\Delta E = E_{\text{pH}=13} - E_{\text{pH}=1}$ .

ionization of  $\text{H}_2\text{O}_2$  at  $25^\circ\text{C}$  ( $\text{pK}_1 = 11.69$ ), the predominant peroxide species at  $\text{pH} = 13$  are  $\text{HO}_2^-$  and at  $\text{pH} = 1$  it is  $\text{H}_2\text{O}_2$ . As depicted in Fig. 2a, the active sites of MnPc/C-300 during the ORR process contain  $\text{Mn}^{n+}$ . The cationic nature of the  $\text{Mn}^{n+}$  active site electrostatically stabilizes anionic  $\text{HO}_2^-$  species in alkaline environments, ensuring the complete  $4e^-$  conversion of  $\text{O}_2$  in alkaline environments. Since  $\text{H}_2\text{O}_2$  molecules are the predominant species in acid medium, the interaction between the active sites and electroneutral  $\text{H}_2\text{O}_2$  is rather limited due to the lack of a strong electrostatic interaction.

### 3.3.3. DFT calculations

We use DFT calculations to verify the crucial function of hydrogen peroxide in the pH-dependent activity (Fig. 5). As illustrated in Fig. 5a, the ORR reaction proceeds via  $\text{O}_2(\text{g})$ ,  $^*\text{OOH}$ ,  $^*\text{O}$ ,  $^*\text{OH}$ , and  $\text{H}_2\text{O}(\text{l})$  to reach  $\text{H}_2\text{O}$ . The electric potential predicted theoretically for  $\text{MnN}_4$  sites according to the free energy diagram of ORR is 0.93 V (Fig. 5b). Theoretical investigations are also conducted to examine the ORR process at various pH levels. For instance, Fig. 5c illustrates the reduction of  $\text{O}_2$  to  $\text{H}_2\text{O}_2$  and  $\text{H}_2\text{O}$  by two and four electrons, respectively. At both  $\text{pH} = 1$  and  $\text{pH} = 13$ ,  $\text{O}_2$  can be readily reduced to water at 0 V. The  $2e^-$  process, which converts  $\text{O}_2$  to  $\text{H}_2\text{O}_2$ , is significantly affected by pH values. Analogous to the  $4e^-$  process,  $\text{O}_2$  can be reduced readily to  $\text{H}_2\text{O}_2$  at a pH of 1. Nevertheless, at a pH of 13, the two-electron reduction to  $\text{H}_2\text{O}_2$  is not thermodynamically favorable, suggesting that the  $\text{H}_2\text{O}_2$  concentration is exceedingly low in alkaline environments. Understanding the pH effects of hydrogen peroxide yields observed in the experiment is facilitated by these results. Furthermore, an analysis is conducted on the catalyzed dissociation of  $\text{H}_2\text{O}_2$  (Fig. 5d and e). To represent acidic conditions, a proton  $\text{H}^+$  is ionically charged with the N atom, whereas an additional proton  $\text{OH}^-$  is ionically charged with the Mn atom to denote alkaline conditions. The dissociation barrier for the HO-OH bond between Mn centers and  $\text{OH}^-$  is 0.67 eV, which is slightly lower than the barrier between N centers and  $\text{H}^+$  (0.92 eV). This discrepancy indicates that dissociation is comparatively simpler to achieve under alkaline conditions as opposed to acidic conditions. In addition, the barrier potential of the subsequent reaction step, which involves the formation of  $\text{H}_2\text{O}$ , is reduced by 1 eV in an alkaline environment. These observations potentially account for the comparatively swift rate at which hydrogen

peroxide decreases in alkalinity.

### 3.4. pH-dependent $\text{H}_2\text{O}_2$ -induced degradation

As discussed above, MnPc/C-300 exhibits stability in alkaline media but failed miserably in acidic medium. Understanding the mechanism responsible for pH-dependent stability would aid in the development of durable Mn-N-C catalysts for use in PEMFCs. In the ORR process with MnPc/C-300 catalysts, the  $\text{H}_2\text{O}_2$  reduction pathway may produce hydroxyl radicals. The high production rate of hydrogen peroxide increases the number of oxygen-containing free radicals. Additionally,  $\cdot\text{OH}$  may react with  $\text{H}_2\text{O}_2$  to produce  $\cdot\text{OOH}$ , another free radical. The  $\cdot\text{OH}$  and  $\cdot\text{OOH}$  radicals both migrate and attack the MnPc molecule. As a molecular probe, 2,20-azino bis(3-ethylbenzthiazoline-6-sulfonate) (ABTS) was used to capture free radicals at  $\text{pH} = 1$  and  $\text{pH} = 13$  to determine the intensity and strength of hydroxyl radical attack on the catalyst at these two pH values [58]. The Fenton influence effects of the catalyst were measured using UV-Vis absorption spectroscopy (Fig. 6a–c). As a solvent, 0.1 M KOH was used to test ABTS,  $\text{ABTS} + \text{H}_2\text{O}_2$ ,  $\text{Mn} + \text{ABTS}$ , and  $\text{Mn} + \text{ABTS} + \text{H}_2\text{O}_2$ . It was discovered that the intensity of absorption at 417 nm does not change, indicating that the Fenton effect of the catalyst was absent at  $\text{pH} = 13$ . However,  $\text{Mn} + \text{ABTS} + \text{H}_2\text{O}_2$  absorbs significantly lighter than ABTS,  $\text{ABTS} + \text{H}_2\text{O}_2$ , and  $\text{Mn} + \text{ABTS}$  at 417 nm when 0.1 M  $\text{HClO}_4$  was used instead as the solvent. After deducting the effects of ABTS and hydrogen peroxide in the  $\text{pH} = 1$  and  $\text{pH} = 13$  solutions, the absorption strength intensity of the medium at  $\text{pH} = 1$  is 0.61, which is considerably greater than 0.018 at  $\text{pH} = 13$ , suggesting that the stronger Fenton effect of Mn-N-C catalysts under the medium at  $\text{pH} = 1$ .

5, 5-dimethyl-1-pyrroline N-oxide (DMPO) was employed as a probe for EPR analysis (Fig. 6d) to confirm whether MnPc/C-300 affects the content of hydroxyl radicals formed under various pH conditions [11]. At  $\text{pH} = 13$ , EPR spectra revealed a four-peak signal with an intensity ratio of 1:2:2:1 that corresponded to the  $\text{-DMPO-OH}$  adduction generated by trapping hydroxyl radicals. However, the catalyst had a more prominent peak at  $\text{pH} = 1$ , indicating that it contained more hydroxyl radicals under acidic conditions. Other ROS than hydroxyl radicals may however have been produced during the hydrogen peroxide treatment, since other DMPO-ROS adducts than  $\text{-DMPO-OH}$  have a shorter lifetime

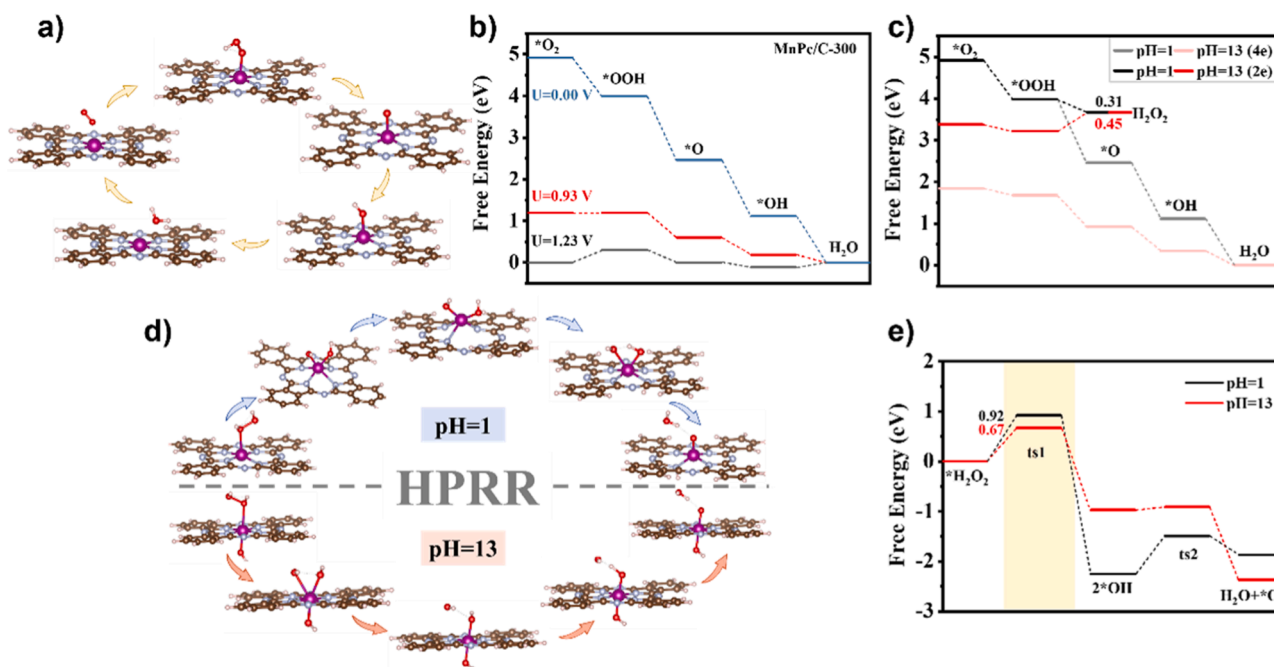


**Fig. 5.** (a) The proposed ORR mechanism on  $\text{MnN}_4$  sites; (b) Gibbs free-energy diagrams on  $\text{MnN}_4$ ; (c) Gibbs free-energy diagrams of ORR on  $\text{MnN}_4$  under 0 V at different pH; (d) Proposed HPRR mechanism on  $\text{MnN}_4$  sites at different pH; (e) Gibbs free-energy diagrams of HPRR on  $\text{MnN}_4$  at  $\text{pH} = 1$  and  $\text{pH} = 13$ .



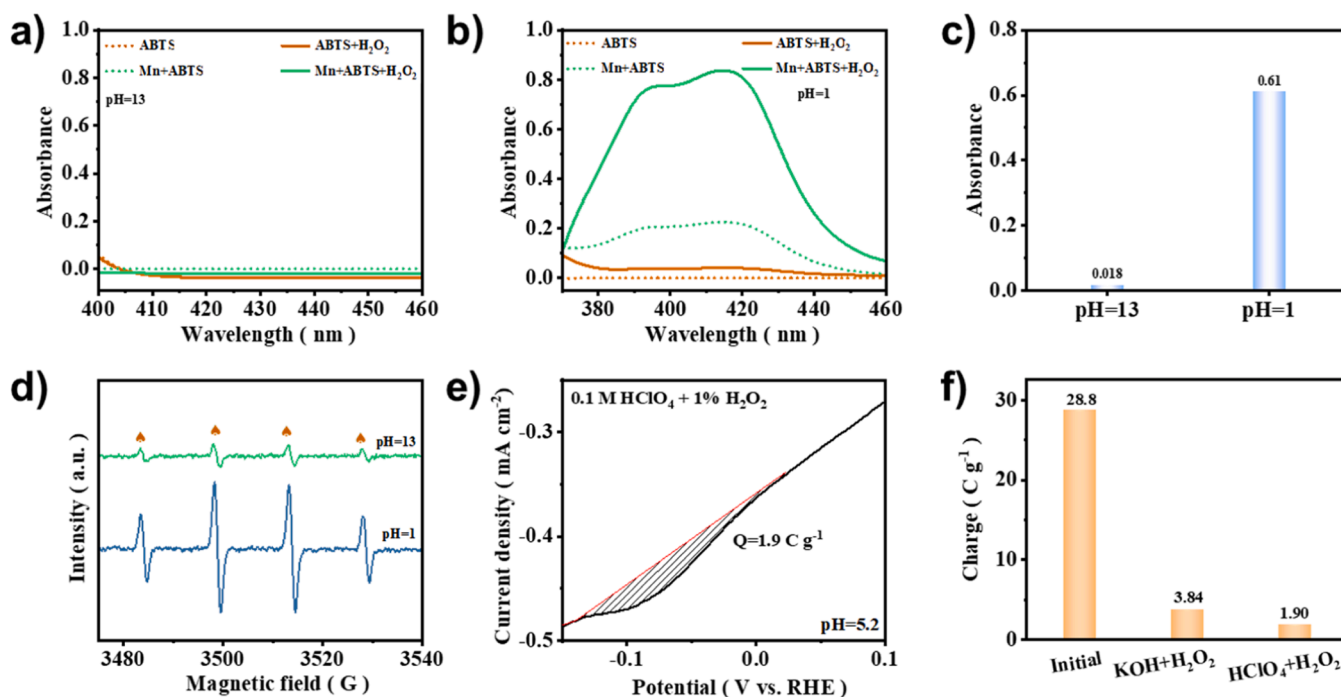


**Fig. 6.** The pH-dependent  $\text{H}_2\text{O}_2$ -induced degradation. The Fenton effect of MnPc/C-300 catalyst was compared under the conditions of pH = 1 and pH = 13. The ultraviolet/visible absorption spectra of ABTS, ABTS +  $\text{H}_2\text{O}_2$ , Mn + ABTS and Mn + ABTS +  $\text{H}_2\text{O}_2$  were tested respectively after 3 min reaction used (a) 0.1 M  $\text{HClO}_4$  and (b) 0.1 M KOH as solvent; (c) the absorption intensity of MnPc/C-300 catalyst at pH = 1 and pH = 13 subtract ABTS +  $\text{H}_2\text{O}_2$  background; (d) the EPR spectra of MnPc/C-300 catalyst with DMPO as free radical scavenger and 0.1 M KOH and 0.1 M  $\text{HClO}_4$  as solvent, respectively; (e) The amount of  $\text{NO}_2^-$  desorption charge of MnPc/C-300 catalyst treated with 0.1 M  $\text{HClO}_4$  containing 1.0 wt%  $\text{H}_2\text{O}_2$ ; (f) The amount of  $\text{NO}_2^-$  desorption charge of different treatment with MnPc/C-300 catalyst at pH = 5.2 acetic acid buffer solution.

and quickly break down to -DMPO-OH adducts. The density of active sites on the surface of the catalyst was determined by  $\text{NO}_2^-$  adsorption (Fig. 6e-f and Fig. S33) in order to investigate the influence of hydrogen peroxide on the catalyst [61,62]. Examine the effect of  $\text{H}_2\text{O}_2$  on site density with  $\text{H}_2\text{O}_2$ -treated 0.1 M KOH or 0.1 M  $\text{HClO}_4$  electrolytes. By measuring the in-situ nitrite desorption charge in acidic and basic electrolytes, the active sites are quantified. At a pH of 5.20, the active site densities of MnPc/C-300 following treatment with alkaline, acidic, alkaline  $\text{H}_2\text{O}_2$  and acidic  $\text{H}_2\text{O}_2$  are  $23.8 \text{ C g}^{-1}$ ,  $12.6 \text{ C g}^{-1}$ ,  $3.84 \text{ C g}^{-1}$ , and  $1.90 \text{ C g}^{-1}$ , respectively. Active site losses range from 17% to 99%. Clearly, the loss of active sites was more severe after treatment with hydrogen peroxide, particularly in acidic solution, indicating a greater activity decline of catalysts, consistent with the stability tests.

Overall, we demonstrate the pH-dependent  $\text{H}_2\text{O}_2$ -induced degradation behavior of MnPc/C-300. Many prior investigations on the Fenton oxidation process have found a pH dependence of the  $\text{H}_2\text{O}_2$ -induced deactivation, which is consistent with our observations [11,63]. By regulating the reaction selectivity or reducing ROS production, PEMFCs could run for longer periods of time. To reduce ROS formation from  $\text{H}_2\text{O}_2$ , it is important to maximize selectivity along the direct four-electron ORR pathway at the molecular level [16,23]. The introduction of secondary catalytic sites where  $\text{H}_2\text{O}_2$  is electrochemically reduced or decomposed to  $\text{H}_2\text{O}$  with a considerably faster kinetics than the Fenton reaction could significantly reduce ROS generation [64]. Due to their pH-dependent stability, Mn-N-C catalysts may also be stabilized during operation by carefully controlling the local pH conditions [11].

### 3.5. Hydroxy radical scavenger

As mentioned previously, durable M-N-C electrocatalysts in PEMFCs could also be accomplished by introducing radical scavengers that react rapidly with ROS near the metal sites. Mixing Pt, Pt-Co alloy, or  $\text{CeO}_x$  particles as radical scavengers with M-N-C can alleviate the

accumulation of  $\text{H}_2\text{O}_2$  [11,65–68]. Adding  $\text{CeO}_2$  to Fe-N-C as a synthetic method to increase the durability of this material is a good illustration of this strategy [67]. It is likely that the absence of efficient radical scavengers operating in the micropores, where the most active  $\text{FeN}_x$  sites are found, is the reason why this method has not yet resulted in greatly increased durability for Fe-N-C catalysts. Instead of using ceria or zirconia nanoparticles, which are less accessible to  $\text{FeN}_x$  sites, Bae et al. employed methanol as a homogenous radical scavenger with equivalent ROS scavenging ability [29]. However, methanol is not an effective radical scavenger for the MnPc/C-300, as shown in Fig. S35. In contrast, IPA significantly increased the durability of MnPc/C-300. As shown in Fig. 7a, after 1 h of operation at pH = 13, the ORR reaction current density in the electrolyte without IPA reduced by about 12% in the durability test performed at a constant potential of 0.6 V, but the ORR activity decreased by less than 3% at 0.1 M KOH with 0.3 M IPA. The increased stability of 0.1 M  $\text{HClO}_4$  has also been noted. The current density approaches zero and the catalyst becomes inactive without the addition of IPA. The IPA's ability to keep the current density at 20% of its initial values in an electrolyte of 0.1 M  $\text{HClO}_4$  suggests that it can be used to effectively prolong the catalyst's lifetime.

As shown in Fig. 7b, MnPc/C-300 worked for 600 s at 0.6 V in pH = 1 electrolyte without the addition of IPA; the current retention only retained the initial 2.2%, which increased to 30% after the addition of IPA, but increased marginally when IPA was added to a pH = 13 electrolyte. In addition, the  $\text{H}_2\text{O}_2$ % percentage of catalysts after stability tests can be decreased by the introduction. The initial yield of hydrogen peroxide in the blank electrolyte is only 10%, but after one hour of operation, it can increase to > 50% (Fig. S36). The production of hydrogen peroxide only climbs to 30% when stability experiments are undertaken in the presence of IPA. In Fig. 7c, the EPR test revealed that after the addition of IPA to a pH = 1 solution, the peak intensity of the hydroxyl radical was significantly lower than without the addition of IPA. IPA could entrap hydroxyl radical and reduce catalyst attack. When

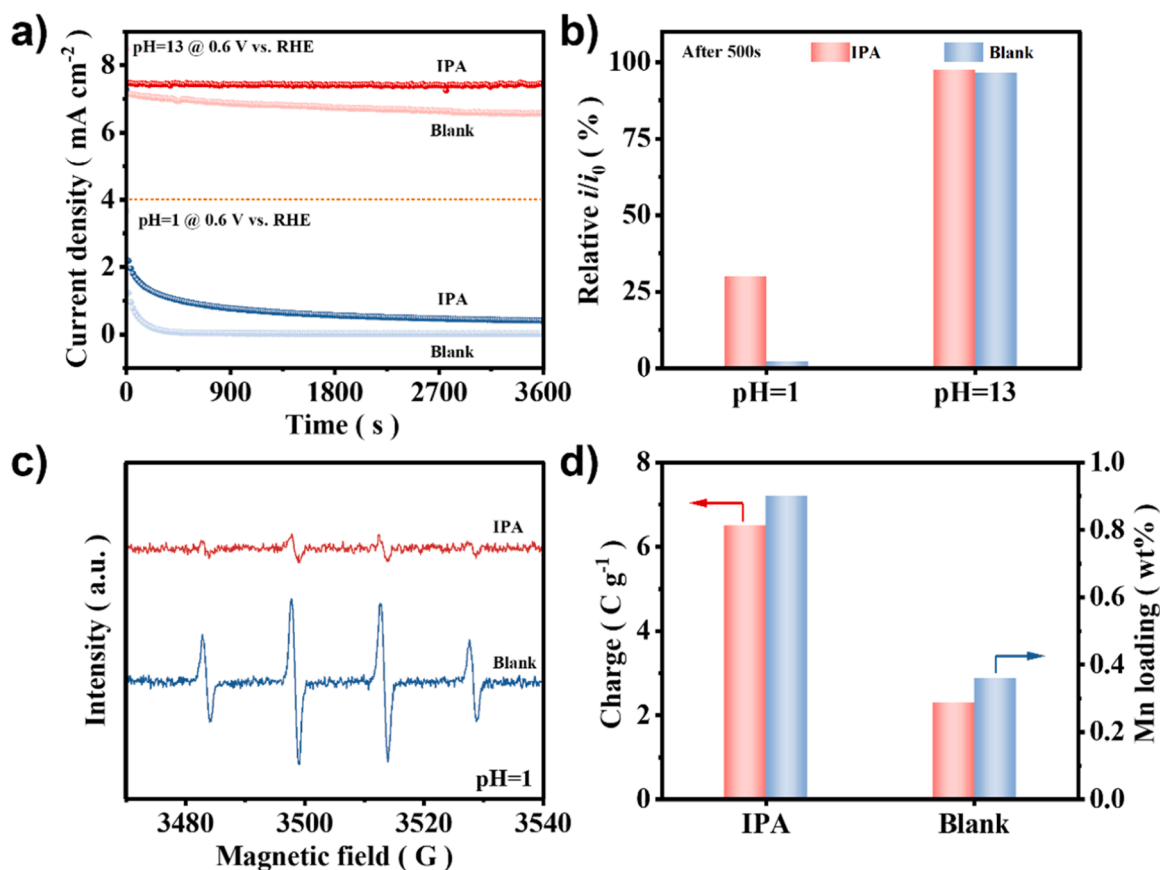


**Fig. 7.** The effect of hydroxyl radical scavenger. (a) Chronoamperometry test of MnPc/C-300 catalyst operating at 0.6 V with pH = 13 and pH = 1 electrolyte with IPA and without IPA; (b) the relative current retention ratio of MnPc/C-300 catalyst at pH = 13 and pH = 1 electrolyte with IPA and without IPA after chronoamperometry test 500 s; (c) the EPR spectra of MnPc/C-300 catalyst with IPA and without IPA used 0.1 M HClO<sub>4</sub> as solvent; (d) the amount of NO<sub>2</sub><sup>-</sup> desorption charge and Mn loading of MnPc/C-300 catalyst at electrolyte pH = 1 after chronoamperometry test with IPA and without IPA.

IPA was introduced to the catalyst, the active site density increased by a factor of 2.8, from 2.3 C g<sup>-1</sup> to 6.5 C g<sup>-1</sup> (Fig. 7d and Fig. S37). In addition, we utilized XPS and ICP-OES to examine the MnPc/C-300 catalyst before and after stability experiments to illustrate how IPA safeguards the active site. Fig. S38 illustrates the alterations that occur at active metal sites. The stability test in the electrolyte with IPA resulted in a reduction of the atom percentage of M-N<sub>4</sub> coordination from 65.4% to 47.8% (Fig. S39). In the absence of IPA, the percentage dropped to 42.7%. According to the data presented in Table S6 and Fig. 7d, the weight percent of Mn for MnPc/C-300, MnPc/C-300 following chronoamperometry experiments in an electrolyte with pH = 1 and without IPA is 1.75%, 0.90%, and 0.36%, respectively. Based on the findings, it can be concluded that IPA can inhibit the loss of active M-N<sub>x</sub> species and the leakage of metal sites.

It is important to acknowledge that stability tests indicate that IPA can only maintain 20% of the initial acidic activity. This improvement is insufficient in comparison to other ROS scavengers, primarily because of the inherent characteristics of MnPc. Despite this, the efficacy of IPA has been illustrated through this improvement. In the future, we intend to investigate the impacts of IPA on additional pyrolyzed M-N-C catalysts.

#### 4. Conclusion

In conclusion, we elucidate the crucial function of hydrogen peroxide in the pH-dependent activity and stability of Mn-N-C. We discovered that the protonation of pyrrolic N cannot explain the enormous difference in catalytic activity between acidic and alkaline media. Using a series of controlled experiments, we demonstrated that the ·OH affinity on Mn centers in alkaline and acid medium differs significantly, and that

the strong pH effects on ORR activity are the consequence of the significantly faster electroreduction kinetics of H<sub>2</sub>O<sub>2</sub> in alkaline media than in acid. The rate of ORR and HPRR is governed by the pH-dependent oxidation of the surface state of Mn centers. The kinetics of HPRR may originate from the surface's inherent affinity for oxygenated species. According to DFT calculations, the dissociation of the HO-OH bond is facilitated in an alkaline environment, resulting in a decrease in the energy required to form H<sub>2</sub>O. For the H<sub>2</sub>O<sub>2</sub>-induced deactivation, a considerable pH dependence is observed in terms of its durability. Corresponding to the loss of active sites, therapies with acidic H<sub>2</sub>O<sub>2</sub> resulted in a significant decrease in activity, whereas alkaline treatments resulted in virtually no deactivation. The concentration of the •DMPO OH spin adduct generated by the Fenton(-like) reactions correlated well with the deactivation trends, indicating that the hydroxyl radical plays a crucial role in the deactivation of Mn-N-C. As a countermeasure, we use IPA as a rapid scavenger of ROS formed near the active sites, which generates a significant increase in stability in both acidic and basic media. Highly effective Mn-N-C catalysts should increase the adsorption of H<sub>2</sub>O<sub>2</sub> and the electrochemical reduction of H<sub>2</sub>O<sub>2</sub> in acidic environments. In addition, minimization of Fenton reagents and rapid removal of ROS generated close to the active sites can be viewed as rational strategies for enhancing the acid resistance of Mn-N-C electrocatalyst. Our work not only provides a novel, substantial, and timely mechanistic understanding of the pH effects, highlighting the critical role of H<sub>2</sub>O<sub>2</sub> in determining the pH dependence of ORR activity and stability of Mn-N-C catalysts, but also paves the way for a more robust catalyst design by swiftly removing hydroxyl radicals formed close to the MnN<sub>4</sub> site.

## CRedit authorship contribution statement

**Li Yuan:** Investigation, Methodology, Data curation, Conceptualization, Writing – original draft. **Miao-Ying Chen:** Methodology, Data curation, Conceptualization, Writing – review & editing. **Bang-An Lu:** Funding acquisition, Resources, Methodology, Conceptualization, Writing – review & editing. **Han-Ran Wu:** Validation, Writing – check. **Jia-Nan Zhang:** Funding acquisition, Supervision.

## Declaration of Competing Interest

The authors declare that they have no known competing financial interests or personal relationships that could have appeared to influence the work reported in this paper.

## Data availability

Data will be made available on request.

## Acknowledgement

This work was financially supported by the National Natural Science Foundation of China (No. 22102156 and U22A20107), China Postdoctoral Science Foundation (2021TQ0295 and 2022M712865), Distinguished Young Scholars Innovation Team of Zhengzhou University (No. 32320275), and Academic Degrees & Graduate Education Reform Project of Henan Province (2021 SJGLX 093Y). We thank the Anhui Absorption Spectroscopy Analysis Instrument Co, Ltd. for XAFS measurements.

## Appendix A. Supporting information

Supplementary data associated with this article can be found in the online version at [doi:10.1016/j.apcatb.2023.123458](https://doi.org/10.1016/j.apcatb.2023.123458).

## References

- [1] X.X. Wang, M.T. Swihart, G. Wu, Achievements, challenges and perspectives on cathode catalysts in proton exchange membrane fuel cells for transportation, *Nat. Catal.* 2 (2019) 578–589, <https://doi.org/10.1038/s41929-019-0304-9>.
- [2] Y. He, G. Wu, PGM-free oxygen-reduction catalyst development for proton-exchange membrane fuel cells: challenges, solutions, and promises, *Acc. Mater. Res.* 3 (2022) 224–236, <https://doi.org/10.1021/accountsmr.1c00226>.
- [3] S. Liu, C. Li, M.J. Zachman, Y. Zeng, H. Yu, B. Li, M. Wang, J. Braaten, J. Liu, H. M. Meyer, M. Lucero, A.J. Kropf, E.E. Alp, Q. Gong, Q. Shi, Z. Feng, H. Xu, G. Wang, D.J. Myers, J. Xie, D.A. Cullen, S. Litster, G. Wu, Atomically dispersed iron sites with a nitrogen-carbon coating as highly active and durable oxygen reduction catalysts for fuel cells, *Nat. Energy* 7 (2022) 652–663, <https://doi.org/10.1038/s41560-022-01062-1>.
- [4] Y. Jia, X. Xiong, D. Wang, X. Duan, K. Sun, Y. Li, L. Zheng, W. Lin, M. Dong, G. Zhang, W. Liu, X. Sun, Atomically dispersed Fe-N<sub>4</sub> modified with precisely located s for highly efficient oxygen reduction, *Nanomicro Lett.* 12 (2020) 116, <https://doi.org/10.1007/s40820-020-00456-8>.
- [5] J. Herranz, F. Jaouen, M. Lefevre, U.I. Kramm, E. Proietti, J.P. Dodelet, P. Bogdanoff, S. Fiechter, I. Abs-Wurmbach, P. Bertrand, T.M. Arruda, S. Mukerjee, Unveiling N-protonation and anion-binding effects on Fe/N/C-catalysts for O<sub>2</sub> reduction in PEM fuel cells, *J. Phys. Chem. C* 115 (2011) 16087–16097, <https://doi.org/10.1021/jp2042526>.
- [6] K. Kumar, L. Dubau, M. Mermoux, J. Li, A. Zitolo, J. Nelayah, F. Jaouen, F. Maillard, On the influence of oxygen on the degradation of Fe-N-C catalysts, *Angew. Chem. Int. Ed.* 59 (2020) 3235–3243, <https://doi.org/10.1002/anie.201912451>.
- [7] X. Wan, X. Liu, J. Shui, Stability of PEM-free fuel cell catalysts: degradation mechanisms and mitigation strategies, *Prog. Nat. Sci. Mater. Int.* 30 (2020) 721–731, <https://doi.org/10.1016/j.pnsc.2020.08.010>.
- [8] L. Gong, J. Zhu, F. Xia, Y. Zhang, W. Shi, L. Chen, J. Yu, J. Wu, S. Mu, Marriage of ultralow platinum and single-atom MnN<sub>4</sub> moiety for augmented ORR and HER catalysis, *ACS Catal.* 13 (2023) 4012–4020, <https://doi.org/10.1021/acscatal.2c06340>.
- [9] Y. Li, M. Chen, B. Lu, J. Zhang, Recent advances in exploring highly active & durable PGM-free oxygen reduction catalysts, *J. Electrochem.* 29 (2023), 2215002, <https://doi.org/10.13208/j.electrochem.2215002>.
- [10] J. Li, S. Chen, N. Yang, M. Deng, S. Ibraheem, J. Deng, J. Li, L. Li, Z. Wei, Ultrahigh-loading zinc single-atom catalyst for highly efficient oxygen reduction in both acidic and alkaline media, *Angew. Chem. Int. Ed. Engl.* 58 (2019) 7035–7039, <https://doi.org/10.1002/anie.201902109>.
- [11] G. Bae, M.W. Chung, S.G. Ji, F. Jaouen, C.H. Choi, Ph effect on the H<sub>2</sub>O<sub>2</sub>-induced deactivation of Fe-N-C catalysts, *ACS Catal.* 10 (2020) 8485–8495, <https://doi.org/10.1021/acscatal.0c00948>.
- [12] Z. Chen, S. Jiang, G. Kang, D. Nguyen, G.C. Schatz, R.P. Van Duyn, Operando characterization of iron phthalocyanine deactivation during oxygen reduction reaction using electrochemical tip-enhanced raman spectroscopy, *J. Am. Chem. Soc.* 141 (2019) 15684–15692, <https://doi.org/10.1021/jacs.9b07979>.
- [13] Y.P. Ku, K. Ehelebe, A. Hutzler, M. Bierling, T. Bohm, A. Zitolo, M. Vorokhta, N. Bibent, F.D. Speck, D. Seeberger, I. Khalakhan, K.J.J. Mayrhofer, S. Thiele, F. Jaouen, S. Cherevko, Oxygen reduction reaction in alkaline media causes iron leaching from Fe-N-C electrocatalysts, *J. Am. Chem. Soc.* 144 (2022) 9753–9763, <https://doi.org/10.1021/jacs.2c02088>.
- [14] X. Xie, C. He, B. Li, Y. He, D.A. Cullen, E.C. Wegener, A.J. Kropf, U. Martinez, Y. Cheng, M.H. Engelhard, M.E. Bowden, M. Song, T. Lemmon, X.S. Li, Z. Nie, J. Liu, D.J. Myers, P. Zelenay, G. Wang, G. Wu, V. Ramani, Y. Shao, Performance enhancement and degradation mechanism identification of a single-atom Co-N-C catalyst for proton exchange membrane fuel cells, *Nat. Catal.* 3 (2020) 1044–1054, <https://doi.org/10.1038/s41929-020-00546-1>.
- [15] J. Li, M. Chen, D.A. Cullen, S. Hwang, M. Wang, B. Li, K. Liu, S. Karakalos, M. Lucero, H. Zhang, C. Lei, H. Xu, G.E. Sterbinsky, Z. Feng, D. Su, K.L. More, G. Wang, Z. Wang, G. Wu, Atomically dispersed manganese catalysts for oxygen reduction in proton-exchange membrane fuel cells, *Nat. Catal.* 1 (2018) 935–945, <https://doi.org/10.1038/s41929-018-0164-8>.
- [16] L. Guo, S. Hwang, B. Li, F. Yang, M. Wang, M. Chen, X. Yang, S.G. Karakalos, D. A. Cullen, Z. Feng, G. Wang, G. Wu, H. Xu, Promoting atomically dispersed MnN<sub>4</sub> sites via sulfur doping for oxygen reduction: unveiling intrinsic activity and degradation in fuel cells, *ACS Nano* 15 (2021) 6886–6899, <https://doi.org/10.1021/acsnano.0c10637>.
- [17] J.H. Zagal, M.T. Koper, Reactivity descriptors for the activity of molecular MN<sub>4</sub> catalysts for the oxygen reduction reaction, *Angew. Chem. Int. Ed.* 55 (2016) 14510–14521, <https://doi.org/10.1002/anie.201604311>.
- [18] H. Meng, F. Jaouen, E. Proietti, M. Lefevre, J.-P. Dodelet, pH-effect on oxygen reduction activity of Fe-based electro-catalysts, *Electrochem. Commun.* 11 (2009) 1986–1989, <https://doi.org/10.1016/j.elecom.2009.08.035>.
- [19] M. Eckardt, K. Sakaushi, A. Lyalin, M. Wassner, N. Hüsing, T. Taketsugu, R. J. Behm, The role of nitrogen-doping and the effect of the pH on the oxygen reduction reaction on highly active nitrided carbon sphere catalysts, *Electrochim. Acta* 299 (2019) 736–748, <https://doi.org/10.1016/j.electacta.2019.01.046>.
- [20] X. Yang, D. Xia, Y. Kang, H. Du, F. Kang, L. Gan, J. Li, Unveiling the axial hydroxyl ligand on Fe-N<sub>4</sub>-C electrocatalysts and its impact on the pH-dependent oxygen reduction activities and poisoning kinetics, *Adv. Sci.* 7 (2020), 2000176, <https://doi.org/10.1002/advsc.202000176>.
- [21] P.K. Gangadharan, A. Pandikassala, S. Kurungot, Toward pH independent oxygen reduction reaction by polydopamine derived 3d interconnected, iron carbide embedded graphitic carbon, *ACS Appl. Mater. Interfaces* 13 (2021) 8147–8158, <https://doi.org/10.1021/acsaami.0c18036>.
- [22] M. Muhyuddin, A. Friedman, F. Poli, E. Petri, H. Honig, F. Basile, A. Fasolini, R. Lorenzi, E. Berretti, M. Bellini, A. Lavacchi, L. Elbaz, C. Santoro, F. Soavi, Lignin-derived bimetallic platinum group metal-free oxygen reduction reaction electrocatalysts for acid and alkaline fuel cells, *J. Power Sources* 556 (2023), 232416, <https://doi.org/10.1016/j.jpowsour.2022.232416>.
- [23] R. Zhang, J.J. Warren, Controlling the oxygen reduction selectivity of asymmetric cobalt porphyrins by using local electrostatic interactions, *J. Am. Chem. Soc.* 142 (2020) 13426–13434, <https://doi.org/10.1021/jacs.0c03861>.
- [24] N. Ramaswamy, S. Mukerjee, Influence of inner- and outer-sphere electron transfer mechanisms during electrocatalysis of oxygen reduction in alkaline media, *J. Phys. Chem. C* 115 (2011) 18015–18026, <https://doi.org/10.1021/jp204680p>.
- [25] K. Wan, Z. Yu, X. Li, M. Liu, G. Yang, J. Piao, Z. Liang, pH effect on electrochemistry of nitrogen-doped carbon catalyst for oxygen reduction reaction, *ACS Catal.* 5 (2015) 4325–4332, <https://doi.org/10.1021/acscatal.5b01089>.
- [26] M.P. Karthikayini, G. Wang, P.A. Bhohe, A. Sheelam, V.K. Ramani, K.R. Priolkar, R. K. Raman, Effect of protonated amine molecules on the oxygen reduction reaction on metal-nitrogen-carbon-based catalysts, *Electrocatalysis* 8 (2016) 74–85, <https://doi.org/10.1007/s12678-016-0341-y>.
- [27] M. Rauf, Y. Zhao, Y. Wang, Y. Zheng, C. Chen, X. Yang, Z. Zhou, S. Sun, Insight into the different ORR catalytic activity of Fe/N/C between acidic and alkaline media: protonation of pyridinic nitrogen, *Electrochem. Commun.* 73 (2016) 71–74, <https://doi.org/10.1016/j.elecom.2016.10.016>.
- [28] G. Liu, X. Li, P. Ganesan, B.N. Popov, Studies of oxygen reduction reaction active sites and stability of nitrogen-modified carbon composite catalysts for pem fuel cells, *Electrochim. Acta* 55 (2010) 2853–2858, <https://doi.org/10.1016/j.electacta.2009.12.055>.
- [29] S. Rojas-Carbonell, K. Artyushkova, A. Serov, C. Santoro, I. Matanovic, P. Atanassov, Effect of pH on the activity of platinum group metal-free catalysts in oxygen reduction reaction, *ACS Catal.* 8 (2018) 3041–3053, <https://doi.org/10.1021/acscatal.7b03991>.
- [30] T. Liu, Y. Wang, Y. Li, How pH affects the oxygen reduction reactivity of Fe-N-C materials, *ACS Catal.* 13 (2023) 1717–1725, <https://doi.org/10.1021/acscatal.2c05540>.
- [31] J. Quilez-Bermejo, K. Strutyński, M. Melle-Franco, E. Morallon, D. Cazorla-Amoros, On the origin of the effect of pH in oxygen reduction reaction for nonpored and edge-type quaternary N-doped metal-free carbon-based catalysts, *ACS Appl. Mater. Interfaces* 12 (2020) 54815–54823, <https://doi.org/10.1021/acsaami.0c17249>.

- [32] Y. Hiraike, M. Saito, H. Niwa, M. Kobayashi, Y. Harada, M. Oshima, J. Kim, Y. Nabae, M.A. Kakimoto, Active site formation mechanism of carbon-based oxygen reduction catalysts derived from a hyperbranched iron phthalocyanine polymer, *Nanoscale Res. Lett.* 10 (2015) 179, <https://doi.org/10.1186/s11671-015-0881-8>.
- [33] J. VandeVondele, M. Krack, F. Mohamed, M. Parrinello, T. Chassaing, J. Hutter, Quickstep: fast and accurate density functional calculations using a mixed gaussian and plane waves approach, *Comput. Phys. Commun.* 167 (2005) 103–128, <https://doi.org/10.1016/j.cpc.2004.12.01>.
- [34] J.P. Perdew, Density-functional approximation for the correlation energy of the inhomogeneous electron gas, *Phys. Rev. B* 33 (1986) 8822–8824, <https://doi.org/10.1103/PhysRevB.33.8822>.
- [35] J.P. Perdew, K. Burke, M. Ernzerhof, Generalized gradient approximation made simple, *Phys. Rev. Lett.* 77 (1996) 3865–3868, <https://doi.org/10.1103/PhysRevLett.77.3865>.
- [36] S. Grimme, J. Antony, S. Ehrlich, H. Krieg, A consistent and accurate ab initio parametrization of density functional dispersion correction (DFT-D) for the 94 elements H–Pu, *J. Chem. Phys.* 132 (2010), 154104, <https://doi.org/10.1063/1.3382344>.
- [37] G. Lippert, P. Michele, H. Jurg, A hybrid gaussian and plane wave density functional scheme, *Mol. Phys.* 92 (1997) 477–488, <https://doi.org/10.1080/002689797170220>.
- [38] J. VandeVondele, J. Hutter, Gaussian basis sets for accurate calculations on molecular systems in gas and condensed phases, *J. Chem. Phys.* 127 (2007), 114105, <https://doi.org/10.1063/1.2770708>.
- [39] S. Goedecker, M. Teter, J. Hutter, Separable dual-space gaussian pseudopotentials, *Phys. Rev. B* 54 (1996) 1703, <https://doi.org/10.1103/PhysRevB.54.1703>.
- [40] G. Henkelman, H. Jónsson, Improved tangent estimate in the nudged elastic band method for finding minimum energy paths and saddle points, *J. Chem. Phys.* 113 (2000) 9978–9985, <https://doi.org/10.1063/1.1323224>.
- [41] X. Zhang, C. Chen, J. Dong, R.X. Wang, Q. Wang, Z.Y. Zhou, S.G. Sun, Comparative study of the oxygen reduction reaction on pyrolyzed FePc in acidic and alkaline media, *ChemElectroChem* 5 (2018) 3946–3952, <https://doi.org/10.1002/celec.201801179>.
- [42] J. Quilez-Bermejo, C. González-Gaitán, E. Morallón, D. Cazorla-Amorós, Effect of carbonization conditions of polyaniline on its catalytic activity towards ORR. Some insights about the nature of the active sites, *Carbon* 119 (2017) 62–71, <https://doi.org/10.1016/j.carbon.2017.04.015>.
- [43] N. Sehlooth, T. Nyokong, Effects of ring substituents on electrocatalytic activity of manganese phthalocyanines towards the reduction of molecular oxygen, *J. Electroanal. Chem.* 595 (2006) 161–167, <https://doi.org/10.1016/j.jelechem.2006.07.011>.
- [44] Q. Hua, K.E. Madsen, A.M. Esposito, X. Chen, T.J. Woods, R.T. Haasch, S. Xiang, A. I. Frenkel, T.T. Fister, A.A. Gewirth, Effect of support on oxygen reduction reaction activity of supported iron porphyrins, *ACS Catal.* 12 (2022) 1139–1149, <https://doi.org/10.1021/acscatal.1c04871>.
- [45] J.A. Behan, A. Iannaci, C. Domínguez, S.N. Stamatina, M.K. Hoque, J. M. Vasconcelos, T.S. Perova, P.E. Colavita, Electrocatalysis of N-doped carbons in the oxygen reduction reaction as a function of pH: N-sites and scaffold effects, *Carbon* 148 (2019) 224–230, <https://doi.org/10.1016/j.carbon.2019.03.052>.
- [46] N. Ramaswamy, U. Tylus, Q. Jia, S. Mukerjee, Activity descriptor identification for oxygen reduction on nonprecious electrocatalysts: linking surface science to coordination chemistry, *J. Am. Chem. Soc.* 135 (2013) 15443–15449, <https://doi.org/10.1021/ja405149m>.
- [47] C. Gonzalez-Gaitan, R. Ruiz-Rosas, E. Morallon, D. Cazorla-Amoros, Relevance of the interaction between the m-phthalocyanines and carbon nanotubes in the electroactivity toward ORR, *Langmuir* 33 (2017) 11945–11955, <https://doi.org/10.1021/acs.langmuir.7b02579>.
- [48] D. Iglesias, A. Giuliani, M. Melchionna, S. Marchesan, A. Criado, L. Nasi, M. Bevilacqua, C. Tavagnacco, F. Vizza, M. Prato, P. Fornasiero, N-doped graphitized carbon nanohorns as a forefront electrocatalyst in highly selective O<sub>2</sub> reduction to H<sub>2</sub>O<sub>2</sub>, *Chem* 4 (2018) 106–123, <https://doi.org/10.1016/j.chempr.2017.10.013>.
- [49] L. Wang, B. Liu, C. Su, W. Liu, C. Kei, K. Wang, T. Perng, Electronic band structure and electrocatalytic performance of Cu<sub>3</sub>N nanocrystals, *ACS Appl. Nano Mater.* 1 (2018) 3673–3681, <https://doi.org/10.1021/acsnm.8b00787>.
- [50] D. Malko, A. Kucernak, Kinetic isotope effect in the oxygen reduction reaction (ORR) over Fe–N/C catalysts under acidic and alkaline conditions, *Electrochem. Commun.* 83 (2017) 67–71, <https://doi.org/10.1016/j.elecom.2017.09.004>.
- [51] T. Tran, M.Y. Song, K.P. Singh, D. Yang, J. Yu, Iron-polypyrrole electrocatalyst with remarkable activity and stability for ORR in both alkaline and acidic conditions: a comprehensive assessment of catalyst preparation sequence, *J. Mater. Chem. A* 4 (2016) 8645–8657, <https://doi.org/10.1039/c6ta01543c>.
- [52] Y. Li, Y. Wang, Z. Zhou, S. Sun, Interface pH regulation to improve ORR performance of FePc catalyst in acid electrolyte, *Electrochem. Commun.* 141 (2022), 107357, <https://doi.org/10.1016/j.elecom.2022.107357>.
- [53] I. Roche, K. Scott, Effect of pH and temperature on carbon-supported manganese oxide oxygen reduction electrocatalysts, *J. Electroanal. Chem.* 638 (2010) 280–286, <https://doi.org/10.1016/j.jelechem.2009.10.030>.
- [54] H. Tian, X. Cui, H. Dong, G. Meng, F. Kong, Y. Chen, L. Peng, C. Chen, Z. Chang, J. Shi, Engineering single MnN<sub>4</sub> atomic active sites on polydopamine-modified helical carbon tubes towards efficient oxygen reduction, *Energy Storage Mater.* 37 (2021) 274–282, <https://doi.org/10.1016/j.ensm.2021.02.017>.
- [55] Z. Lin, H. Huang, L. Cheng, Y. Yang, R. Zhang, Q. Chen, Atomically dispersed mn within carbon frameworks as high-performance oxygen reduction electrocatalysts for zinc–air battery, *ACS Sustain. Chem. Eng.* 8 (2019) 427–434, <https://doi.org/10.1021/acssuschemeng.9b05713>.
- [56] J. Shi, S. Deng, X. Hu, X. Sun, S. Zhou, L. Fan, W. Cai, J. Li, Interconnected porous structural construction of Mn- and N-doped carbon nanosheets for fuel cell application, *Energy Fuels* 36 (2022) 8432–8438, <https://doi.org/10.1021/acs.energyfuels.2c02061>.
- [57] Y. Chen, X. Hua, S. Chen, Theoretical study of stability of metal-n<sub>4</sub> macrocyclic compounds in acidic media, *Chin. J. Catal.* 37 (2016) 1166–1171, [https://doi.org/10.1016/s1872-2067\(15\)61082-8](https://doi.org/10.1016/s1872-2067(15)61082-8).
- [58] E. Luo, H. Zhang, X. Wang, L. Gao, L. Gong, T. Zhao, Z. Jin, J. Ge, Z. Jiang, C. Liu, W. Xing, Single-atom Cr–N<sub>4</sub> sites designed for durable oxygen reduction catalysis in acid media, *Angew. Chem. Int. Ed.* 58 (2019) 12469–12475, <https://doi.org/10.1002/anie.201906289>.
- [59] F. Hasché, M. Oezaslan, P. Strasser, T.-P. Feller, Electrocatalytic hydrogen peroxide formation on mesoporous non-metal nitrogen-doped carbon catalyst, *J. Energy Chem.* 25 (2016) 251–257, <https://doi.org/10.1016/j.jechem.2016.01.024>.
- [60] X. Jing, D. Cao, Y. Liu, G. Wang, J. Yin, Q. Wen, Y. Gao, The open circuit potential of hydrogen peroxide at noble and glassy carbon electrodes in acidic and basic electrolytes, *J. Electroanal. Chem.* 658 (2011) 46–51, <https://doi.org/10.1016/j.jelechem.2011.04.025>.
- [61] D. Malko, A. Kucernak, T. Lopes, Performance of Fe–N/C oxygen reduction electrocatalysts toward NO<sub>2</sub>, NO, and NH<sub>2</sub>OH electroreduction: from fundamental insights into the active center to a new method for environmental nitrite destruction, *J. Am. Chem. Soc.* 138 (2016) 16056–16068, <https://doi.org/10.1021/jacs.6b09622>.
- [62] D. Xia, C. Yu, Y. Zhao, Y. Wei, H. Wu, Y. Kang, J. Li, L. Gan, F. Kang, Degradation and regeneration of Fe–N<sub>x</sub> active sites for the oxygen reduction reaction: the role of surface oxidation, Fe demetallation and local carbon microporosity, *Chem. Sci.* 12 (2021) 11576–11584, <https://doi.org/10.1039/d1sc03754d>.
- [63] C.H. Choi, H.-K. Lim, M.W. Chung, G. Chon, N. Ranjbar Sahraie, A. Altin, M.-T. Sougrati, L. Stievano, H.S. Oh, E.S. Park, F. Luo, P. Strasser, G. Dražić, K.J. J. Mayrhofer, H. Kim, F. Jaouen, The achilles’ heel of iron-based catalysts during oxygen reduction in an acidic medium, *Energy Environ. Sci.* 11 (2018) 3176–3182, <https://doi.org/10.1039/c8ee01855c>.
- [64] G. Yang, J. Zhu, P. Yuan, Y. Hu, G. Qu, B.A. Lu, X. Xue, H. Yin, W. Cheng, J. Cheng, W. Xu, J. Li, J. Hu, S. Mu, J.N. Zhang, Regulating Fe-spin state by atomically dispersed Mn–N in Fe–N–C catalysts with high oxygen reduction activity, *Nat. Commun.* 12 (2021) 1734, <https://doi.org/10.1038/s41467-021-21919-5>.
- [65] X. Cheng, X. Jiang, S. Yin, L. Ji, Y. Yan, G. Li, R. Huang, C. Wang, H. Liao, Y. Jiang, S. Sun, Instantaneous free radical scavenging by CeO<sub>2</sub> nanoparticles adjacent to the Fe–N<sub>4</sub> active sites for durable fuel cells, *Angew. Chem. Int. Ed. Engl.* 62 (2023), e202306166, <https://doi.org/10.1002/anie.202306166>.
- [66] P. Trogadas, J. Parrondo, V. Ramani, Platinum supported on CeO<sub>2</sub> effectively scavenges free radicals within the electrolyte of an operating fuel cell, *Chem. Commun.* 47 (2011) 11549–11551, <https://doi.org/10.1039/c1cc15155j>.
- [67] C. Qiu, R. Gao, Y. Guo, J. Qin, G. Zhang, Y. Song, CeO<sub>2</sub> nanoparticles boosted Fe–N–C sites derived from dual metal organic frameworks toward highly active and durable oxygen reduction reaction, *Adv. Mater. Interfaces* 9 (2022), 2200852, <https://doi.org/10.1002/admi.202200852>.
- [68] F. Xiao, Q. Wang, G.-L. Xu, X. Qin, I. Hwang, C.-J. Sun, M. Liu, W. Hua, S. H.-w. Wu, J.-C. Zhu, J.-G. Li, Y. Wang, D. Zhu, Z. Wu, M. Wei, K. Gu, M. Amine, Shao, Atomically dispersed Pt and Fe sites and Pt–Fe nanoparticles for durable proton exchange membrane fuel cells, *Nat. Catal.* 5 (2022) 503–512, <https://doi.org/10.1038/s41929-022-00796-1>.